ARTICLE IN PRESS

Nature Communications

https://doi.org/10.1038/s41467-026-70388-1

Article in Press

Self-polymerized polyphenol-based platform for the management of dry eye pathogenesis

Received: 16 May 2025

Accepted: 10 February 2026

Cite this article as: Wang, Z., Lv, Z., Ge, Y. *et al.* Self-polymerized polyphenol-based platform for the management of dry eye pathogenesis. *Nat Commun* (2026). https://doi.org/10.1038/s41467-026-70388-1

Zixin Wang, Zeen Lv, Yuxuan Ge, Ruiyang Xue, Fang Wu, Haijie Han & Yin Wang

We are providing an unedited version of this manuscript to give early access to its findings. Before final publication, the manuscript will undergo further editing. Please note there may be errors present which affect the content, and all legal disclaimers apply.

If this paper is publishing under a Transparent Peer Review model then Peer Review reports will publish with the final article.

ARTICLE IN PRESS

© The Author(s) 2026. **Open Access** This article is licensed under a Creative Commons Attribution-NonCommercial-NoDerivatives 4.0 International License, which permits any non-commercial use, sharing, distribution and reproduction in any medium or format, as long as you give appropriate credit to the original author(s) and the source, provide a link to the Creative Commons licence, and indicate if you modified the licensed material. You do not have permission under this licence to share adapted material derived from this article or parts of it. The images or other third party material in this article are included in the article's Creative Commons licence, unless indicated otherwise in a credit line to the material. If material is not included in the article's Creative Commons licence and your intended use is not permitted by statutory regulation or exceeds the permitted use, you will need to obtain permission directly from the copyright holder. To view a copy of this licence, visit http://creativecommons.org/licenses/by-nc-nd/4.0/.

ARTICLE IN PRESS

Self-polymerized Polyphenol-based Platform for the Management of Dry Eye Pathogenesis

Zixin Wang[#1], Zeen Lv[#2], Yuxuan Ge[3], Ruiyang Xue[1], Fang Wu[2], Haijie Han*[2], Yin Wang*[1]

---

[1]Engineering Research Center of Cell & Therapeutic Antibody, Shanghai Frontiers Science Center of Drug Target Identification and Delivery, Shanghai Key Laboratory for Antibody-Drug Conjugates with Innovative Target, National Key Laboratory of Innovative Immunotherapy, School of Pharmaceutical Sciences, Shanghai Jiao Tong University, Shanghai, 200240, China.

[2]Eye Center, the Second Affiliated Hospital, School of Medicine, Zhejiang University, Zhejiang Provincial Key Laboratory of Ophthalmology, Zhejiang Provincial Clinical Research Center for Eye Diseases, Zhejiang Provincial Engineering Institute on Eye Diseases, Hangzhou, 310009, China.

[3]Shanghai Jiao Tong University Affiliated Sixth People's Hospital South Campus, Shanghai, 201499, China.

✉email: hanhj90@zju.edu.cn; yinwang@sjtu.edu.cn

[#]These authors contributed equally: Zixin Wang, Zeen Lv

ARTICLE IN PRESS

ARTICLE IN PRESS

Abstract

The management of ocular surface inflammation, particularly in conditions like dry eye disease (DED), remains challenging due to multiple pathogenic causes and ocular barriers. Traditional eye drops usually provide transient and partial symptom relief, necessitating combined therapies to break the vicious cycle of oxidative stress and inflammation. To surmount these limitations, a polyphenol-based eye drop is developed via the self-polymerization of rosmarinic acid in the presence of hyaluronic acid, followed by co-assembly with cerium ions to afford monodispersed RHC NPs. To enhance the ocular retention efficiency, thiol groups are further decorated on NPs (termed as *s*-RHC NPs). In two mouse models of DED, topical administration of *s*-RHC NPs leads to comprehensive relief of symptoms, including inflammatory response suppression, corneal epithelial defect repair, and tear secretion recovery. We envision that this work might facilitate the treatment of DED and inspire the design of polyphenol-based nanoparticles via a self-polymerization strategy.

ARTICLE IN PRESS

Introduction

Dry eye disease (DED), a global health issue characterized by tear deficiency and sustained ocular inflammation, significantly impacts people's quality of life[1,2]. Its prevalence is escalating due to overuse of electronic screens[3]. First-line therapies for this disease primarily involve artificial tears for lubrication and anti-inflammatory agents like cyclosporine to regulate the ocular surface immune response. However, their efficacy is limited and compromised by rapid tear clearance, demanding frequent administration[4,5]. Moreover, the presence of ocular barriers like mucus layers, and the conjunctival epithelium, impedes drug penetration as well[6]. Without timely interventions, DED would generate an oxidative stress-inflammation vicious cycle, including hyperosmolarity, oxidative damage, inflammation, and cell apoptosis to further aggravate the situation[7]. Therefore, alternative therapies with sustained efficacy are highly required.

As sufficient drug concentrations at lesion sites are essential for efficacy, researchers have exploited various platforms to enhance ocular drug penetration and retention for DED[8,9]. Nevertheless, the penetration of delivered drugs is compromised by mucus. It is rich in mucin, and abundantly contains negatively charged sulfate and sialic acid groups, along with a protein backbone interspersed with cysteine-rich regions[10,11]. Leveraging these features, some surface-engineered nanomaterials capable of interacting with mucus have

ARTICLE IN PRESS

been developed[12-14]. Zhang et al. designed chitosan-coated liposomes that enhanced drug retention via electrostatic interactions with negatively charged mucin[14], though excessive positive charge on nanomaterials risks cytotoxicity. Alternatively, thiol functionalization is another strategy to augment muco-adhesion by forming disulfide linkages with cysteine-rich subdomains[15]. For instance, Lai et al. fabricated a multifunctional nanoceria wrapped with thiolated gelatin, which boosted corneal retention, cellular uptake, and bioactivity[16].

Natural phenols, marked by their phenolic and conjugated structures, exhibit outstanding reactive oxygen species (ROS)-scavenging and anti-inflammatory properties[17,18]. Despite their medical potential, several defects hinder clinical translation: (i) poor aqueous solubility obstructs drug administration, (ii) the anti-oxidative capacity, especially for small-molecular phenols, is restricted by the low content of phenol moieties[19,20]. As far as we know, apart from the well-established synthetic routes for polydopamine, report on chemically polymerized nano-polyphenols from natural phenols remains underexplored[21-23].

Herein, we engineer a facile strategy to construct an artificial polyphenol platform with satisfactory anti-oxidative and anti-inflammatory properties for DED treatment. Initially, rosmarinic acid (RosA) is converted into polymerized RosA (*p*RosA) through self-polymerization. However, thus-formed *p*RosA without a template is neither stable nor uniform. Hence, hyaluronic acid (HA) is incorporated into the polymerized system and then co-assembles with cerium ions (Ce^{3+}) to afford uniformly dispersed nanoparticles, termed as RHC NPs (Fig. 1a). To enhance muco-adhesive ability, thiol groups are coated onto RHC NPs via a condensation reaction (abbreviated as *s*-RHC NPs). Specifically, the phenolic hydroxyl and carboxyl groups presented on the RosA moieties interact mildly with mucins, while thiols on *s*-RHC NPs act as “claws”, forming stronger interactions via disulfide bonds (Fig. 1b). Moreover, Ce^{3+} not only behaves as a cross-linker but also as a ROS-scavenging and anti-inflammatory nanozyme[24,25], thanks to the redox cycle between Ce^{3+} and Ce^{4+} due to the presence of oxygen vacancies[26-28]. Conclusively, the *s*-RHC NPs are hypothesized to efficiently bind to the ocular tissue by thiol “claws”, exerting multifunctional effects such as alleviating ocular inflammation, promoting corneal epithelial repair, and moisturizing to cure DED.

ARTICLE IN PRESS

Results

Design and characterizations of *s*-RHC NPs

*p*RosA was initially synthesized via an oxidative polymerization from free RosA by sodium periodate ($NaIO_4$), with a color change from colorless to reddish-brown (Supplementary Fig. 1a). In situ Fourier transform infrared spectroscopy (FTIR) detection of RosA polymerization showed intensified peaks between 1450 cm^{-1} and 1750 cm^{-1}, reflecting enhanced conjugation of C=C bonds (benzene rings) and C=O bonds (ester moieties) (Fig. 2a and Supplementary Fig. 1b). Additionally, peak shifts in the 1140–1190 cm^{-1} range confirmed perturbations in C−O stretching caused by polymerization (Supplementary Fig. 1c, d). Ultraviolet-visible spectroscopy (UV-vis) and transmission electron microscopy (TEM) confirmed the formation of nano-sized *p*RosA, which had comparable bioactivity to monomeric RosA while exhibiting non-uniform dispersion (PDI = 0.984) (Supplementary Fig. 2). To improve the stability and morphology, RosA was then polymerized in the presence of HA, which acted as a stabilizer, followed by the co-assembly with Ce^{3+} at 37 °C. Interestingly, mono-dispersed spheres gradually formed via co-assembly as the mass ratio of RosA:HA, molecular weight of HA, and reaction temperature were adjusted (Fig. 2b and Supplementary Figs. 3-5).

To enhance muco-adhesion, thiols were decorated onto RHC NPs (Fig. 2c). Four thiolated RHC NPs were prepared with varying thiol contents (0%, 3.4%, 4.7%, and 8.2%), which were designated as RHC, s_1-RHC, s_2-RHC, and s_3-RHC, respectively. Thiol functionalization made zeta potentials increase from -49.4 ± 0.89 mV to -29.6 ± 2.79 mV, and slightly decreased the hydrodynamic size (Fig. 2d, e). Subsequently, the muco-adhesive ability of thiol-decorated NPs was elucidated by incubating them with mucin at 37°C. As shown in Fig. 2f, g, all three thiolated RHC NPs had a higher affinity with mucin than bare analogs. We reckoned that disulfide bonds formed between thiolated NPs and cysteine-rich mucin subdomains likely mediated strong adhesion, different from weaker interactions including hydrogen bonds and Van der Waals forces (Fig. 2c). Interestingly, mucin-binding behaviors were not proportional to thiol contents, as s_2-RHC NPs had the strongest muco-adhesive ability compared with s_1- or s_3-RHC NPs. It was speculated that mucin-binding may peak at the intermediate thiol density (s_2-RHC) because excessive -SH groups (e.g., s_3-RHC) likely induced NP self-aggregation, competing with the mucin interaction. This self-aggregation behavior was identified by TEM (Supplementary Fig. 6). Thus, s_2-RHC NPs (denoted as *s*-RHC NPs later) were selected for further experiments.

ARTICLE IN PRESS

Particle trajectories in mucin solutions were also analyzed using Nanoparticle Tracking Analysis (NTA). RHC NPs diffused freely across mucin with longer trajectories, while *s*-RHC NPs showed constrained movement (Fig. 2h, i and Supplementary Movies 1-4). Mean square displacements (MSD) and effective diffusion coefficient (D_{eff}) analysis over 15 s revealed significantly higher values for RHC NPs, further confirming the mucoadhesive properties of *s*-RHC NPs (Supplementary Fig. 7)[29]. Then, the in vivo muco-adhesive properties of these NPs were evaluated. As shown in Fig. 2j, k, free fluorescein (*Flu*) was rapidly cleared within 5 min, while *Flu*-RHC and *Flu*-*s*-RHC NPs showed prolonged retention, with *Flu*-*s*-RHC maintaining the strongest fluorescence after 20 min. To avoid the potential interference from reduced blinking and tear evaporation in anaesthetized mice, corneal tissues from non-anaesthetized mice were also examined. *Flu*-*s*-RHC NPs displayed 4.5-fold higher fluorescence intensity than free fluorescein and 2.3-fold higher than *Flu*-RHC after 10 min (Supplementary Fig. 8), further confirming their superior ocular surface binding capabilities.

Elemental compositions and distributions of *s*-RHC NPs were subsequently identified (Supplementary Fig. 9). In Fig. 2l, elements carbon (C), nitrogen (N) and sulfur (S) had a wider distribution than the other elements, proving the successful coating of thiols on the surface of RHC NPs. X-ray photoelectron spectroscopy (XPS) spectra identified the chemical compositions and valence states of Ce in *s*-RHC NPs (Fig. 2m, n): the peaks at 880.2, 885.1, 894.7, and 903.6 eV belonged to Ce^{3+}, and the peaks at 881.9, 887.1, 899.3, 901.1, 902.8, and 916.7 eV represented Ce^{4+} [7,30]. Ce species existed in both +3 (78.9%) and +4 (21.1%) valence states, possibly due to the oxidation of Ce^{3+} by solubilized oxygen in aqueous solutions. Besides, the radical-trapping behavior of NPs was evaluated. *s*-RHC NPs exhibited concentration-dependent ABTS•+ scavenging activity, achieving an 88.2% scavenging rate at 250 μg mL^{-1} (Supplementary Fig. 10). The Methylene blue assay confirmed their effective elimination of ·OH generated by Mn^{2+} and hydrogen peroxide (H_2O_2) (Fig. 2o). Additionally, the ferric reducing ability of plasma (FRAP) assay revealed that the total antioxidant activity (TOA) of RHC NPs was 1.34-fold and 2.09-fold higher than that of RosA and Ce^{3+}, respectively (Fig. 2p), indicating that TOA was primarily driven by polyphenols, with a partial contribution from Ce^{3+}. Notably, thiol-functionalization did not compromise the TOA of *s*-RHC NPs. Furthermore, we intriguingly observed a ROS-responsive morphological change in *s*-RHC NPs under TEM (Fig. 2q), where smaller spheres were non-uniformly distributed on the surface of NPs in 30 min exposed to H_2O_2. We surmised that

ARTICLE IN PRESS

this phenomenon was due to the partial transition of Ce species from cerium (III) ions to cerium (IV) oxide. And the ROS-stimulated morphological change would augment the specific surface area of NPs, further boosting their anti-oxidative capacity.

Cytoprotective and ROS-scavenging efficacy mediated by *s*-RHC NPs

While *s*-RHC NPs could form disulfide linkages with mucus, this poses a dilemma, as it may impede their penetration into corneal cells. To explore their penetration behaviors, we employed a human corneal epithelial cell (HCECs) monolayer transwell model to mimic the ocular surface (Fig. 3a). The results revealed that disulfide bond formation hindered *s*-RHC NPs internalization at the very beginning, whereas the endocytosis recovered gradually, reaching similar levels to both the mucin-RHC and bare *s*-RHC groups (Fig. 3b and Supplementary Fig. 11). Combined with fluorescence images (Fig. 3c), we conclude that *s*-RHC NP-mucus interactions are robust yet reversible, without compromising endocytosis into the corneal layer. Next, HCECs were pre-incubated with inhibitors (chlorpromazine, amiloride, genistein) to investigate the uptake mechanism. Pre-incubation with amiloride and genistein reduced internalization, while chlorpromazine had no significant impact (Fig. 3d), indicating that *s*-RHC NPs entered HCECs mainly through macro-pinocytosis and caveolae-mediated endocytosis.

DED involves prolonged exposure to atmospheric oxygen and tear film instability, which potentially triggers overexpression of ROS[31]. In this regard, eliminating excess ROS may help protect eyes from oxidative stress-induced injury. We thus estimated the anti-oxidative capacity of *s*-RHC NPs by H_2O_2-stimulated HCECs. As illustrated in Supplementary Fig. 12a, H_2O_2-stimulated HCECs generated a large amount of ROS detected by the 2′,7′-dichlorodihydrofluorescein diacetate (DCFH-DA) probe. The ROS-scavenging capacity of free RosA was slightly better than that of Ce^{3+} ions, while these two formulations showed cooperative effects in both NPs groups. Moreover, *s*-RHC NPs could mitigate H_2O_2 or hyperosmolarity-induced cell death evidenced by cell counting kit-8 (CCK-8) assay (Supplementary Fig. 12b, c), as well as the apoptosis assay validated by flow cytometry (Fig. 3e, f). Moreover, ROS imbalance in eye tissues typically rises lipid peroxidation and elevates the level of malondialdehyde (MDA)[32]. As expected, H_2O_2-treated HCECs exhibited increased levels of MDA, whereas treatments with free RosA or Ce^{3+} could somehow alleviate lipid peroxidation. Notably, both NPs treatments reduced MDA by 3-fold versus the H_2O_2 group (Fig. 3g). Likewise, the activities of another

ARTICLE IN PRESS

anti-oxidative enzyme superoxide dismutase (SOD), almost recovered to normal levels following NPs treatments (Fig. 3h).

Next, we performed RNA sequencing (RNA-seq) on HCECs to analyze early changes in oxidative signaling pathways after *s*-RHC NPs treatment. Principal components analysis (PCA) (Fig. 3i) and Volcano plots (Fig. 3j) showed significant transcriptional variations between the control and NPs groups. A total of 254 differentially expressed genes (DEGs) were identified, with 139 genes up-regulated and 115 genes down-regulated. Notably, *s*-RHC NPs suppressed a series of cellular stress and apoptosis-related genes like *PPP1R15A*, *JUN*, and *GADD45A*, etc.[33-35]. The representative hierarchical clustering heatmaps (Supplementary Fig. 13) further revealed an up-regulation of anti-apoptotic BCL-2 family, while heat shock proteins (HSPs), which are activated by cellular disorders like heat, oxidative stress, and DNA damage[36,37], were markedly down-regulated after NPs treatment. Then, we conducted Kyoto Encyclopedia of Genes and Genomes (KEGG) analysis to elucidate the signaling pathways regulated by the aforementioned DEGs. As depicted in Fig. 3k, down-regulation in pathways like p53 signaling pathway (Supplementary Fig. 14), and IL-17 signaling pathway (Supplementary Fig. 15) were observed. The gene set enrichment analysis (GSEA) also identified that *s*-RHC NPs attenuated IL-17 signaling pathways by declining pro-inflammatory cytokine genes like *IL-17B*, *IL-17RB*, and *CXCL3* (Supplementary Fig. 16)[38]. Besides, downregulation of base excision repair pathways was observed in *s*-RHC groups as well (Supplementary Fig. 17), indicating the potential nucleus-protective effect of *s*-RHC NPs. After analyzing the transcriptome of H_2O_2-treated HCECs with or without *s*-RHC NPs protection, we subsequently investigated the downstream protein profiles using proteomics. NPs treatment induced distinct protein clustering, as shown by PCA analysis in Supplementary Fig. 18. To further validate the cytoprotective efficacy of *s*-RHC NPs, we analyzed the functions of identified proteins in HCECs using Gene Ontology (GO) annotation. Top-ranked terms included oxidative stress and immune response (Fig. 3l), and differential proteins regulating ROS responses and growth factor activity were up-regulated (Supplementary Fig. 19).

Noteworthy, the protein numbers of “intracellular organelle” term also exhibited a significant change (Fig. 3l). It inspired us to assess the total protein changes of HCECs based on the subcellular localization. Fig. 3m showed that differential proteins were primarily localized in the nucleus (34.18%), cytoplasm (19.62%), and plasma membrane (11.39%), with the nucleus having the highest proportion. Considering the previous GSEA

ARTICLE IN PRESS

data from RNA-seq which indicated base excision repair behavior of *s*-RHC NPs, we further explored their DNA-protective effects. DNA damage is often accompanied by the formation of phospho-histone H2A.X (γ-H2A.X), a biomarker for double-strand breaks[39]. As ROS mediates DNA damage, we detected γ-H2A.X foci in the nucleus (Fig. 3n). The foci in H_2O_2-treated HCECs considerably increased compared to normal cells; by contrast, *s*-RHC NPs treatment reduced γ-H2A.X foci formation by 80.5% due to the synergistic effect of RosA and Ce^{3+} (Fig. 3o). Collectively, these results provide evidence for the robust cytoprotective efficacy of *s*-RHC NPs against H_2O_2-induced oxidative damage.

M1-to-M2 repolarization effect of *s*-RHC NPs

In the progression of DED, environmental or endogenous irritants would trigger ocular inflammatory disorders. Macrophages, prevalent at inflammatory sites, predominantly maintain the M1-like phenotype in unresolved inflammation areas[40,41]. Thus, modulating inflammation and macrophage repolarization are key focuses of treating DED. Before assessing the anti-inflammatory capacity of NPs, their internalization and uptake pathways were first evaluated by macrophage cell lines (RAW264.7 cells). As presented in Fig. 4a, b, RAW264.7 cells efficiently internalized *s*-RHC NPs within 0.5 h, primarily through clathrin-mediated endocytosis and micropinocytosis (Fig. 4c).

The immunomodulatory effects of NPs were then tested by coculturing different formulations with lipopolysaccharide (LPS)-induced M1-like phenotype RAW264.7 cells. Phalloidin staining revealed that RHC and *s*-RHC NPs changed RAW264.7 cells from an irregular polygonal shape with multiple pseudopodia to a spindle shape (highlighted by white arrows), indicating the repolarization from M1-to-M2 phenotype by NPs (Fig. 4d). To quantify this effect, flow cytometry was employed to measure the phenotypes of macrophages treated with different formulations. Fig. 4e, f demonstrated that the anti-inflammatory ability of Ce^{3+} ions was stronger than that of RosA, as the ratios of M2/M1-phenotype cell were 0.96±0.29 and 0.39±0.12, respectively. The synergy formulations of RosA and Ce^{3+}, i.e., RHC NPs and *s*-RHC NPs, exhibited the strongest repolarization efficiency on RAW264.7 cells. Meanwhile, enzyme-linked immunosorbent assay (ELISA) identified that the intervention of NPs increased the secretion of M2-phenotype marker Transforming Growth Factor-β (TGF-β), while the levels of two representative pro-inflammatory cytokines, including Tumor Necrosis Factor-α (TNF-α) and Interleukin-6 (IL-6), were reduced to normal (Fig. 4g). Additionally, the expression of

ARTICLE IN PRESS

inducible nitric oxide synthase (iNOS) in macrophages was assessed because it facilitated the liberation of large quantities of NO to elicit damage and inflammation[42]. As revealed by the immunofluorescence images in Fig. 4h, incubation of *s*-RHC NPs diminished iNOS expression, along with raised levels of Arginase-1 (Arg1) which denoted weakened M1-like phenotype. The M1-to-M2 repolarization capability of *s*-RHC NPs was also confirmed by declined NO generation via the Griess assay (Fig. 4i).

In addition to the findings regarding macrophage polarization status described above, we further monitored whether LPS stimulation would arouse not only inflammation but also ROS. As shown in Fig. 4j and Supplementary Fig. 20, low-dose of LPS (0.25 μg mL^{-1}) did not significantly affect oxidative stress levels, while higher concentrations increased the percentage of ROS-positive RAW264.7 cells by 7.3% (0.5 μg mL^{-1}) and 16.4% (1 μg mL^{-1}). This suggested that persistent inflammation, a hallmark of the vicious cycle in DED, would exacerbate oxidative stress as well. Parallelly, the decreased cellular ROS level shown in Fig. 4k identified the cyto-protective effects of NPs on RAW264.7 cells. Together, these results demonstrated that *s*-RHC NPs could ameliorate inflammation and oxidative stress in macrophage models.

In vivo therapeutic effect of *s*-RHC NPs

Encouraged by the potent anti-oxidative and anti-inflammatory properties of *s*-RHC NPs in vitro, we used two different DED models to validate the in vivo therapeutic efficacy. As illustrated in Fig. 5a, evaporative DED models were established following a 7-day benzalkonium chloride (BAK) administration[43], and corneal fluorescein staining images were recorded to trace the defect area of the corneal epithelium (Supplementary Fig. 21). Restasis®, a clinically established cyclosporine A emulsion that suppresses T cell-mediated inflammation, was used as a positive benchmark to assess the efficacy of *s*-RHC NPs. Corneal fluorescein staining (Fig. 5b, c) revealed persistent epithelial defects in the Saline group (scores >10 for 7 days), while RosA and Ce^{3+} treatments showed partial improvement. Notably, *s*-RHC NPs demonstrated superior efficacy, achieving negligible staining on Day 3, outperforming both monotherapies and Restasis®. Beyond epithelial repair, key DED parameters—tear secretion (Schirmer test) and tear film stability (TBUT)—were quantitatively assessed. Schirmer tests showed that RosA (2.74 ± 0.51 mm) and Ce^{3+} (2.62 ± 0.61 mm) treatments moderately improved tear production compared to the Saline group, while *s*-RHC NPs exhibited remarkable restorative capacity, elevating tear production to 4.58 ± 0.60 mm, a level that was significantly higher than the

ARTICLE IN PRESS

Restasis® group (Fig. 5d). Similar trends were observed on TBUT, indicating the synergistic efficacy of *s*-RHC in restoring tear film stability (Fig. 5e). According to these clinical indicators, *s*-RHC NPs outperformed the commercial drug Restasis® in 7 days. This difference may be attributed to the fact that Restasis® exerts its anti-inflammatory effects through immunomodulation, which typically requires a longer duration to manifest[44].

Subsequently, hematoxylin-eosin (H&E) and periodic acid schiff (PAS) staining were used to assess histomorphological changes in ocular tissues following various interventions. In healthy corneas, epithelial cells are dense and organized with consistent thickness, and the stromal layer is tight without inflammatory cell infiltration. However, the superficial corneal epithelium exhibited signs of fracture induced by BAK (the Saline group), resulting in diminished thickness and irregular morphology[45,46]. Compared with the RosA and Ce^{3+} group, the corneas of both NPs treated groups showed a more pronounced recovery. Nonetheless, there was no significant difference between RHC and *s*-RHC groups on the final corneal epithelial thickness (Fig. 5f). We reckoned that the muco-adhesive ability enhanced by thiolation was more beneficial in the recovery of DED in the early stage, while both groups gradually recovered as time elapsed (after 3 days). Moreover, healthy eyes had abundant PAS-positive goblet cells in the conjunctival fornix, whereas these were severely depleted in the BAK-treated Saline group. In contrast, *s*-RHC treatment effectively restored the goblet cell population, even more effectively than Restasis®, which has been reported to have a beneficial effect on goblet cell recovery (Fig. 5g)[47]. Additionally, H&E staining of the lacrimal glands indicated that *s*-RHC significantly mitigated the pathological alterations in the lacrimal gland, with more organized acinar cells and uniform nuclei positioned at the basal region.

As the progression of DED is linked to the ROS-mediated apoptosis and inflammation[18,48], specific markers were evaluated by immunohistochemistry (Fig. 5h-l). After DED induction, the Saline group exhibited a high level of oxidative stress, while eyes administrated with RosA or Ce^{3+} showed a moderate relief. Meanwhile, the *s*-RHC group displayed a marked reduction in ROS levels, surpassing the RHC group and approaching the Restasis® group, suggesting that the muco-adhesive capability further enhanced the effectiveness of RHC NPs in trapping radicals. Similarly, treatment with *s*-RHC NPs significantly reduced the numbers of MMP-9- and terminal deoxynucleotidyl transferase-mediated dUTP nick-end labeling (TUNEL)-positive cells, along with a more pronounced decrease in the key inflammatory cytokine IL-6. We subsequently conducted the whole-mount immunofluorescence staining of the cornea to assess the effect of *s*-RHC NPs

ARTICLE IN PRESS

on macrophages (Fig. 5m). The results showed clear changes in macrophage polarization after different treatments. Expression of both CD86 and CD206 was the lowest in the healthy control group, whereas CD86 expression was markedly increased in the saline-treated group, indicating a predominance of the pro-inflammatory M1-like phenotype. In contrast, treatment with *s*-RHC significantly lowered CD86 expression and elevated CD206 levels. Quantitatively, the M2/M1 phenotype fluorescence intensity ratio increased to 2.89 ± 0.76, supporting a shift toward the anti-inflammatory M2 phenotype (Fig. 5n). Together, these data suggested *s*-RHC NPs acted as an effective radical and inflammation trapper in evaporative DED models.

Unlike BAK which induces dry eye by corneal toxicity, scopolamine (SCOP), as a non-selective muscarinic antagonist, inhibits tear production by blocking lacrimal gland pathways[49]. Thus, we further validated the therapeutic efficacy of *s*-RHC NPs on SCOP-induced DED. After 7 days of SCOP injection, the tear-deficient dry eye model was established (Fig. 6a). As illustrated in Fig. 6b, the ocular surface of modeling mice's eyes on Day 0 exhibited a diffuse punctate fluorescence pattern, distinctly different from the one induced by BAK. This is because SCOP-induced model mimics Sjögren's syndrome, causing chronic inflammation, and compromising corneal epithelium integrity[50]. After 5 days of treatments, monotherapies (RosA or Ce^{3+}) and Restasis® had mild effects, while *s*-RHC NPs demonstrated the fastest recovery, significantly reducing fluorescence retention (Fig. 6c and Supplementary Fig. 22a). Apart from fluorescein staining, tear-related assessments were also conducted (Fig. 6d, e). The tear volume in the RosA and Ce^{3+} groups showed a little recovery compared to the Saline group, as a result of their limited curative effects and short retention time in tears. In contrast, RHC NPs had a higher Schirmer test result of 4.14 ± 0.47 mm. The *s*-RHC NPs, as expected, exerted an optimal treatment efficacy with a tear volume of 4.94 ± 0.53 mm. The results of TUBT also had a similar tendency over 7 days (Supplementary Fig. 22b, c), suggesting that *s*-RHC NPs could effectively mitigate the lacrimal gland toxicity induced by SCOP.

Then, the therapeutic efficacy of the NPs was further confirmed by histomorphological examination. In SCOP-modeling mice, the corneal epithelial layer had severe atrophy and thinned to approximately 27.57 ± 5.07 μm (Fig. 6f, g). After treatments, RosA and Ce^{3+} restored the thickness to 35.52 ± 0.85 μm and 34.66 ± 0.55 μm, respectively. The RHC and *s*-RHC groups demonstrated significant recovery, comparable to that of commercial drug group. Goblet cells, which secrete mucins to lubricate the ocular surface, were significantly reduced in SCOP-induced DED. Nevertheless, the *s*-RHC group demonstrated a marked restoration of the

ARTICLE IN PRESS

goblet cell area, indicating a more effective therapeutic response than those by other groups. Furthermore, histological analysis of lacrimal glands in SCOP-injected mice revealed severe atrophy, extensive acinar nuclear loss, and prominent inflammatory cell infiltration in the Saline group. Inflammatory damage also induced pronounced vacuolization within the acini. Following the treatment with Ce^{3+}, the acinar cells showed partial recovery; a few vacuoles remained in the acinar cells following RosA treatment. The morphology of the lacrimal glands in both NPs groups exhibited the best recovery, with acinar cells being uniformly arranged, plump in shape, and nuclei showing proper distribution (Fig. 6g). Finally, immunofluorescence staining of the corneal epithelium was performed. As depicted in Fig. 6h-l, the ROS, MMP-9, TUNEL, and IL-6 levels were reduced following the treatment of RosA or Ce^{3+}. Among all these groups, *s*-RHC demonstrated non-inferior efficacy to Restasis® in suppressing oxidative stress and preventing corneal epithelial apoptosis, suggesting its strong potential in mitigating SCOP-induced DED.

ARTICLE IN PRESS

Safety evaluation

For preclinical assessment of DED therapeutic agents, it's essential to ensure their biosafety. The cytotoxicity of RHC NPs and *s*-RHC NPs on RAW264.7 cells and HCECs were first evaluated. Remarkably, the viabilities of both cell lines incubated with NPs were maintained at a high level (>85%), as evidenced by both CCK-8 and live/dead cell staining assay (Supplementary Fig. 23, 24). The NPs also showed superior stability (Supplementary Fig. 25) and low hemolysis rate even when the concentration was as high as 200 μg mL^{-1} (Supplementary Fig. 26). These findings suggested that *s*-RHC NPs is a biocompatible candidate with good stability for in vivo DED treatments.

Next, ocular surface irritation was assessed in animals immediately following drug administration. Anterior segment optical coherence tomography (OCT) on healthy mice administered with both NPs revealed no significant short-term changes in corneal thickness, and the corneal integrity remained well preserved (Supplementary Fig. 27). H&E staining also confirmed normal corneal epithelial thickness, intact epithelium, and well-arranged epithelial cells after NPs treatments (Supplementary Fig. 28). Together, these findings indicate that the tested drugs induce minimal ocular surface irritation in vivo and demonstrate favorable biocompatibility. Finally, the long-term ocular and systemic biocompatibility of *s*-RHC NPs was further assessed to confirm their suitability for extended use. Weekly anterior segment OCT over four weeks showed

ARTICLE IN PRESS

no significant change in corneal thickness of mice (Fig. 6m), and body weights remained within the normal range throughout the study (Fig. 6n). H&E staining revealed normal corneal structure with tightly packed epithelial cells, and that of major organs (heart, liver, spleen, lungs, and kidneys) showed no pathological alterations (Supplementary Fig. 29). Besides, long-term biocompatibility was further evaluated on rabbits. Slit-lamp examination on rabbit eyes received with *s*-RHC on Day 0, 7, 14, 21, and 28 revealed no abnormalities such as conjunctival congestion, corneal injury, or anterior chamber opacity (Fig. 6o). Taken together, the results confirm that *s*-RHC NPs possess excellent short- and long-term biosafety, with no signs of adverse effects either locally or systemically.

Discussion

In this study, we have successfully utilized a self-polymerization strategy to obtain polymerized RosA, which was subsequently assembled with HA and Ce^{3+} to form the polyphenol RHC NPs. To enhance their muco-adhesive efficiency, the NPs were decorated with thiol groups, termed as *s*-RHC NPs. The ROS-triggered morphological change of *s*-RHC NPs derived from Ce^{3+}/Ce^{4+}, along with the multiple catechols in *p*RosA moieties, endowed the NPs with superior radical-scavenging and anti-inflammatory behaviors. This platform performed well in both in vitro cellular experiments and in vivo mouse models with two types of DED models. The results demonstrated the *s*-RHC NPs could repolarize inflammatory macrophages, suppress oxidative stress, and enhance epithelial regeneration, demonstrating faster therapeutic effects than the clinical benchmark, Restasis®. Compared with other DED treatments, our study introduced a facile strategy to obtain artificial polyphenol nanoparticles as eye drops, bypassing the need for traditional chemical drugs. Utilizing natural phenols as nano-drugs via a self-polymerization strategy provides a fresh perspective in creating convenient and integrated therapies for DED, along with other diseases associated with ROS and inflammation. As the monomer (i.e., rosmarinic acid) could be expanded to other phenols, we believe the approach adopted here provides a facile way to on-demand maximize efficacy of other functional segments for DED treatments.

ARTICLE IN PRESS

Methods

Materials

Sodium hyaluronate (mW ≈ 30 kDa) was purchased from Bloomage Biotech. (Beijing, China). Cerium (III) nitrate hexahydrate, hydrogen peroxide solution (30 wt.% H_2O_2), amiloride hydrochloride, genistein, chlorpromazine, and paraformaldehyde solution (4 wt.% PFA) were purchased from Titan Biotech. (Shanghai, China). 1-(3-Dimethylaminopropyl)-3-ethylcarbodiimide hydrochloride (EDC), 1-hydroxybenzotriazole (HOBT), mercaptolethylamine hydrochloride, ethylene diamine tetraacetic acid (EDTA), 2',7'-dichlorodihydrofluorescein diacetate (DCFH-DA), and Annexin V-fluorescein isothiocyanate (FITC) apoptosis detection kit were purchased from Aladdin Biochem Tech. (Shanghai, China). Benzalkonium chloride (BAK) and scopolamine (SCOP) were purchased from Sigma-Aldrich (St. Louis, USA). Rosmarinic acid was purchased from Meryer Biotech. (Shanghai, China). ABTS free radical scavenging capacity assay kit was purchased from Solarbio Biotech. (Beijing, China). 10 mM phosphate buffered saline (PBS), Dulbecco's modified eagle medium (DMEM), and 1% penicillin/streptomycin were purchased from Thermo Fisher Scientific (MA, USA). 10% Fetal bovine serum (FBS)-Premium was purchased from NEWZERUM (Christchurch, New Zealand). Triton-X 100 solution, Actin-Tracker Red-594, Bradford protein assay kit, and live/dead viability/cytotoxicity assay kit were purchased from Beyotime Biotech. (Shanghai, China). Cell counting kit-8 (CCK-8) was purchased from Life-iLab (Shanghai, China). Mucin, lipopolysaccharide (LPS), and Total antioxidant capacity assay kit with ferric reducing ability of plasma (FRAP) method were purchased from Yuanye Bio-Tech. (Shanghai, China). 4',6-diamidino-2-phenylindole (DAPI) was purchased from Yeasen Biotech. (Shanghai, China). Enzyme-linked immunosorbent assay (ELISA) kits of Transforming Growth Factor-β (TGF-β), Tumor Necrosis Factor-α (TNF-α), and Interleukin-6 (IL-6) were purchased from Solarbio Biotech. (Beijing, China). Restasis® (0.05% cyclosporine) was purchased from Allergan Sales (Dublin, IE).

The primary and secondary antibodies used in study were listed as follows: p-histone H2A.X antibody (Ser 139) (Santa Cruz Biotech., Cat #sc-517348, monoclonal, Lot #F1523, 1:1000), inducible nitric oxide synthase (iNOS) antibody (Biobend, Cat #KY5993, polyclonal, Lot #F158402, 1:200), arginase-1 (Arg1) antibody (Biobend, Cat #BQA6565, polyclonal, Lot #WY5101A, 1:200), interleukin-6 (IL-6) monoclonal antibody (Proteintech, Cat #83747-5-RR, polyclonal, Lot #23009609, 1:200), matrix metallopeptidase-9 (MMP-9) polyclonal antibody (Proteintech., Cat #10375-2-AP, polyclonal, Lot #00126508, 1:200),

ARTICLE IN PRESS

phycoerythrin (PE)-conjugated anti-mouse cluster of differentiation 86 (CD86) antibody (Biolegend, Cat #159204, monoclonal, Lot #B376302, 1:200), allophycocyanin (APC)-conjugated anti-mouse CD206 antibody (BioLegend, Cat #141708, monoclonal, Lot #B385870, 1:200), multi-rAbTM coraLite® plus 488-goat anti-mouse recombinant secondary antibody (H+L) (Proteintech., Cat #RGAM002, Lot #20001275, 1:1000), multi-rAbTM coraLite® plus 594-goat anti-mouse recombinant secondary antibody (H+L) (Proteintech, Cat #RGAM0004, Lot #20001241, 1:1000).

Cells and animals

Mouse macrophage cells (RAW264.7, Cat #TIB-71) and Human Corneal Epithelial Cells (HCECs, Cat #PCS-700-010) were purchased from American Type Culture Collection (ATCC). The animal experiments conducted in this study were carried out according to the guidelines set forth by the Association for Research in Vision and Ophthalmology Statement for the Use of Animals in Ophthalmic and Vision Research, as well as the Animal Care and Use Committee at Zhejiang University. Approval for these experiments was obtained from the Animal Ethics Committee at the Second Affiliated Hospital, School of Medicine, Zhejiang University (Approval number: 2024-284). All wild-type C57BL/6J mice (*Mus musculus,* 6-8 weeks, 20 ± 2 g, male) were provided by SLAC Laboratory Animal Co., Ltd (Shanghai, China). Mice were housed under specific pathogen-free (SPF) conditions. The animal room was maintained at 22–24 °C with a 12 h light/12 h dark cycle; humidity was controlled within the institutional standard range of 30–70%. Food and water were provided with unrestricted access to food and water. All wild-type New Zealand white rabbits (*Oryctolagus cuniculus*, 6-8 weeks, 2-2.5 kg, male) were provided by SLAC Laboratory Animal Co., Ltd (Shanghai, China). Similarly, the rabbits were housed in a standard environment with constant temperature and a regular light/dark cycle with ad libitum access to food and water.

Synthesis of *p*RosA, RHC NPs, and *s*-RHC NPs

10 mg of RosA was dissolved in 500 μL of dimethyl sulfoxide (DMSO) and added with 30 mL of ultrapure water. Next, 7.5 mg of $NaIO_4$ was injected quickly, and the reaction mixture was vigorously stirred at room temperature (r.t.) overnight to form *p*RosA. To prepare monodisperse RHC NPs, 50 mg of HA·Na was added into RosA solution as a stabilizer, followed by injection of 7.5 mg of $NaIO_4$. 15 mg of $Ce(NO_3)_3{\cdot}6H_2O$ was

ARTICLE IN PRESS

subsequently added dropwise to form RHC NPs. The resultant solution was centrifuged at 10000 g for 3 times for final purification. To prepare thiolated RHC NPs, RHC NPs were suspended in 20 mL of ultrapure water with 1-(3-dimethylaminopropyl)-3-ethylcarbodiimide/1-hydroxybenzotriazole (EDC/HOBT) added to activate the free carboxyl groups of HA. Varying amounts of mercaptolethylamine hydrochloride (0.42 mg, 0.85 mg, or 1.70 mg) were added and stirred at r.t. overnight. The obtained products were purified by dialysis against deionized water (molecular weight cutoff = 3500 Da), and denoted *s*$_1$-RHC, *s*$_2$-RHC (denoted as *s*-RHC), and *s*$_3$-RHC NPs, respectively. Fluorescein labeled RHC and *s*-RHC NPs were prepared using a similar procedure, in which 500 μL of fluorescein (2 mg mL^{-1} in DMSO) was added simultaneously with the injection of $Ce(NO_3)_3 \cdot 6H_2O$ during the formation of the RHC to form *flu*-RHC NPs or *flu*-*s*-RHC NPs.

Interactions between the NPs and mucin

RHC, *s*$_1$-RHC, *s*$_2$-RHC, and *s*$_3$-RHC NPs were incubated with different concentrations of mucin in a shaker at 37 °C for 1 h. Then, the NPs were removed by centrifugation at 10000 g for 20 min, and the unbound mucin was quantified by Bradofrd Protein Assay Kit. Similarly, particle trajectories of RHC NPs and *s*-RHC NPs when incubating with mucin were detected by Nanoparticle Tracking Analysis (NTA). The tracking image movies were sequenced by PotPlayer (Intercept images per 500 ms, a total of 30 interceptions), and the speed and paths of NPs were analyzed by ImageJ plugin manual tracking functions. The average MSD and D_{eff} values were determined according to the following formula:

$$\text{MSD}(\Delta t) = \left[X_{(t+i)} - X_{(t)}\right]^2 + \left[Y_{(t+i)} - Y_{(t)}\right]^2 \quad (1)$$

$$D_{\text{eff}} = \frac{\text{MSD}}{4i} \quad (2)$$

Where *X* and *Y* represent the NPs coordinate at a certain time point, and *i* denotes the time scale [51,52].

Cellular internalization profiles and pathway investigations

The HCEC monolayer Transwell model was established as follows: HCECs were first seeded in the lower chamber and incubated for 24 h. Fluorescein-labelled NPs (*Flu*-RHC, *Flu*-*s*-RHC) were pre-incubated with

ARTICLE IN PRESS

mucin at 37 °C for 30 min and then added to the upper chamber, followed by co-culture with HCECs for specified time periods. FITC-positive cells were quantitatively analyzed using a LSRFortessa X-20 flow cytometer (BD Biosciences) and visualized by confocal laser scanning microscopy (LSM900, ZEISS). The endocytosis pathway of *s*-RHC NPs was conducted by the addition of common inhibitors. Prior to the addition of NPs, HCEC and RAW264.7 cells were preincubated with a certain concentration of inhibitors for 30 min at 37 °C (30 μM chlorpromazine / 320 μM amiloride / 100 μM genistein). Then, 20 μg mL^{-1} of NPs were incubated with cells for another 4 h. Positive cells were further measured quantitatively via a LSRFortessa X-20 flow cytometer (BD Bioscience).

Intracellular cytotoxicity assay

CCK-8 assay was used to assess the cytotoxicity of RHC NPs and *s*-RHC NPs. In brief, HCECs and RAW264.7 cells were seeded into 96-well plates at a density of 3×10^3 per well and incubated for 24 h. Subsequently, cells were incubated with fresh cell culture medium containing different concentrations of NPs for 24 h. Then, the cells were rinsed once with phosphate buffered saline (PBS), replaced with 100 μL of fresh cell culture medium containing 10% of CCK-8, and incubated for another 1 h. Ultimately, the absorbance of the solution at the wavelength of 450 nm was detected. Live/dead fluorescent imaging of treated cells was achieved by Calcein-AM and PI staining by upright fluorescence microscope (BX53, Olympus).

The cell viability was calculated by the following equation:

$$\text{Cell viability} = \frac{(OD_{450nm}\text{of the sample} - OD_{450nm}\text{of the blank})}{(OD_{450nm}\text{of the control} - OD_{450nm}\text{of the blank})} \times 100\% \quad (3)$$

In vitro anti-oxidative ability of *s*-RHC NPs

CCK-8 assay was initially applied to assess the cytoprotective effects of *s*-RHC NPs against H_2O_2-induced cell damage. HCECs were seeded into 96-well plates and treated with 400 μM H_2O_2 for 12 h. Subsequently, cells were incubated with fresh cell culture medium containing 20 μg mL^{-1} of *s*-RHC NPs for 12 h. To mimic tear hyperosmotic stress (HS), we supplemented the cell culture medium with 100 mM sodium chloride (NaCl). Cells were first incubated with fresh cell culture medium containing NaCl and then replaced with medium containing 20 μg mL^{-1} of NPs for 12 h. CCK-8 kit was applied to access the cell viability. For ROS observations, HCECs were seeded in 24-well plates and pre-treated with 400 μM H_2O_2 for 12 h (except for the Control

ARTICLE IN PRESS

group). After that, cells were incubated with different formulations: (1) Control (replaced with fresh cell culture medium), (2) H_2O_2 (replaced with fresh cell culture medium), (3) RosA, (4) Ce^{3+}, (5) RHC, (6) *s*-RHC (RosA: 5.72 μg mL^{-1}, Ce^{3+}: 1.74 μg mL^{-1} at a final concentration) for 12 h, followed by staining with 10 μM DCFH-DA in serum-free Dulbecco's modified eagle medium for 30 min. Finally, cells were washed with PBS again and observed by the BX53 upright fluorescence microscope. The anti-oxidative effect of NPs was also evaluated by flow cytometry: after incubation, the cell precipitates were resuspended in 0.5 mL of PBS, stained with Annexin-V-FITC/PI, and analyzed by LSRFortessa X-20 flow cytometer (BD Bioscience).

Quantification of cellular anti-oxidative activity

HCECs were seeded in 6-well plates and the following treatments were the same as above. Harvested cells were lysed at 4 °C using NP-40 cell lysis buffer for 10 min. Then, the pyrolysis products were centrifuged at 10000 g for 10 min to collect the supernatant for subsequent antioxidative assays and total protein level tests via a BCA assay. The corresponding sample quantification was performed using MDA, and CAT detection kits.

mRNA-sequencing and proteomics

HCECs were seeded in 12-well plates and pre-treated with 400 μM H_2O_2 for 12 h. After that, cells were incubated with different formulations: (1) Control (replaced with fresh cell culture medium), (2) NPs (treated with *s*-RHC) for 12 h, Then, the total RNA from the cells was harvested using TRIzol reagent. After enrichment and purification of the obtained mRNA, Agilent 2100 bioanalyzer was used to assess these mRNA. Then, these mRNA was sequenced on an Illumina Novaseq platform. The web-based NovoMagic data analysis platform was used for raw data variance modeling and statistical analyses, with a combination of $|\log_2 \text{Fold Change}| > 0.5$ and p value < 0.05 used as the cutoff to select significantly differentially expressed genes. To examine the total proteomes, HCECs were treated as the same way shown above. The total protein qualitative and relative quantitative analysis were done by Data-independent acquisition (DIA) patterns. Proteins exhibiting a $|\log_2 \text{FoldChange}| > 1.2$ and a p value < 0.05 were considered differentially expressed. Subcellular localization analysis was also conducted to identify differentially expressed proteins. Both mRNA-sequencing and proteomics were completed with the help of Novogene Co., Ltd (Beijing, China).

ARTICLE IN PRESS

In vitro anti-inflammatory effect of *s*-RHC NPs

RAW264.7 cells were seeded in 24-well plates overnight and then exposed to 1 μg mL^{-1} of LPS for 12 h to obtain the active M1-like macrophages (except for the Control group). After that, cells were treated with different formulations: (1) Control (replaced with fresh cell culture medium), (2) LPS (replaced with fresh cell culture medium), (3) RosA, (4) Ce^{3+}, (5) RHC, (6) *s*-RHC (RosA: 5.72 μg mL^{-1}, Ce^{3+}: 1.74 μg mL^{-1} at a final concentration) for another 12 h. The M1-like and M2-like macrophages were labelled with CD86 and CD206 antibodies, which were analyzed by LSRFortessa X-20 flow cytometer (BD Bioscience).

Immunofluorescence

RAW264.7 cells were seeded into confocal dishes and exposed to 1 μg mL^{-1} of LPS for 12 h. HCECs were seeded in confocal dishes and pre-treated with 400 μM H_2O_2 for 12 h. After different treatments, cells were fixed with 4% paraformaldehyde for 15 min and permeabilized with 0.3% Triton X-100 for 30 min at r.t. Subsequently, the treated cells were incubated with primary antibodies at 4 °C for 12 h, followed by conjugation with CoraLite488-labelled secondary antibodies/CoraLite594-labelled secondary antibodies at r.t. for 1 h. After staining with DAPI for 5 min, these cells were observed through the confocal laser scanning microscope (LSM900, ZEISS).

ARTICLE IN PRESS

Measurement of anti-inflammatory and pro-inflammatory indicators

Briefly, RAW264.7 cells were seeded into 24-well plates and exposed to 1 μg mL^{-1} of LPS for 12 h. After incubating with different formulations for 12 h, the amount of nitrite accumulation in the culture medium, an indicator of NO production, was measured by Griess assay. Similarly, the levels of IL-6, TNF-α, and TGF-β were determined by the corresponding ELISA kits.

Ocular surface retention evaluation of *s*-RHC NPs

To fully assess the precorneal retention time of *s*-RHC NPs, in vivo imaging under anesthesia and cryopreserved sections of mice eyeballs without anesthesia was conducted. Fluorescein was loaded into *s*-RHC NPs to obtain *Flu*-*s*-RHC NPs. For in vivo imaging, the mice were anaesthetized using intraperitoneal administration of 300 mg kg^{-1} sodium pentobarbital. Subsequently, 5 μL of free fluorescein, *Flu*-RHC, and *Flu*-

ARTICLE IN PRESS

s-RHC (10 mM of fluorescein at a final concentration) were instilled into the right eyes. The fluorescence intensity of the mouse eye was recorded using an in vivo imaging system (Lumina LT, PerkinElmer) at specific time points (0, 1, 5, 10, and 20 min) with excitation/emission wavelengths of 488 nm/520 nm. For cryopreserved section imaging, the same eye drops of free fluorescein, *Flu*-RHC, and *Flu*-*s*-RHC, as mentioned earlier, were applied to the corneal surfaces of conscious DED mice. The mice were euthanized precisely at 2 and 10 min after administration, and their eyeballs were removed and rapidly frozen in dry ice with optimum cutting temperature compound (4583, SAKURA). 7 μm of frozen sections were cut and observed under a fluorescence microscope. The image intensity was quantified using ImageJ software.

Establishment of the DED model and therapeutic evaluation of *s*-RHC NPs

The evaporative DED model mice were set according to previously reported methods[7]. To be specific, the evaporative DED model mice were induced by administering 5 μL of 0.2% w/v BAK eye drops to each eye twice daily for 7 consecutive days. Differently, SCOP was used to interfere with tear production[18]. Each mouse was intraperitoneally injected with 200 μL of 0.25% w/v SCOP four times a day over a seven-day period. Apart from the healthy mice (group (1)), the evaporative DED model and aqueous deficient DED model mice were randomly divided into five groups and treated with 2 μL of topical eye drops twice daily: (2) 0.9% Saline (w/v), (3) RosA, (4) Ce^{3+}, (5) RHC, (6) *s*-RHC (RosA: 200 μg mL^{-1}, Ce^{3+}: 60.8 μg mL^{-1} at a final concentration), (7) Restasis®.

After establishing the DED model, the therapeutic efficacy was assessed on the final induction day (designated Day 0) and on treatment days 1, 3, 5, and 7. The Schirmer Test utilized phenol red-impregnated cotton threads (Tianjin Jingming Tech.) was employed to quantify the tear volume in mice. TBUT was measured by utilizing cobalt blue light under a slit lamp (YZ5T, 66 Vision-Tech.) to identify the moment when the black dot first became visible. For fluorescein sodium staining, a small volume (2 μL) was administered into the conjunctival sac on each eye's side. Following this, corneal fluorescein staining was conducted using cobalt blue light under slit-lamp examination. Staining was scored from 0 to 4 for each of four corneal quadrants according to the following scale: 0, no staining; 1, slight punctate staining (<30 spots); 2, significant punctate staining (>30 spots, non-confluent); 3, diffuse staining; 4, positive plaque formation[41]. After being undergone for 7 days of therapeutic intervention, the mice were euthanized for subsequent comprehensive

ARTICLE IN PRESS

examination. The eyeballs of the mice were collected for histological staining using H&E, PAS, and immunofluorescence techniques. The corneal thickness in each HE-stained eyeball section was measured at three equally spaced points, and the mean value was calculated as the representative measurement for that sample.

Statistical analyses

The statistical analyses were conducted using GraphPad Prism 10. In the case of multiple group comparisons, a two-tailed one-way ANOVA with Tukey's multiple comparisons test was employed. In the case of two group comparisons, a two-sided, unpaired Student's *t* test was performed. All results are presented as the mean ± SD, as indicated. Statistical significance was denoted by the specific *p* value, while non-significant results were indicated as ns.

Data availability

The RNA sequencing data generated in this study are deposited in the NCBI's Sequence Read Archive (SRA) under accession code PRJNA1369795 [https://www.ncbi.nlm.nih.gov/sra/PRJNA1369795]. The proteomics data generated in this study are deposited in the NCBI's Sequence Read Archive (SRA) under accession code IPX0014408002 [https://www.iprox.cn/page/project.html?id=IPX0014408000]. Source data are available for Figs. 2d-i, 2k, 2m-p, 3b,d, 3f-h, 3o, 4c, 4f-j, 5c-f, 5i-l, 5n, 6c-f, 6i-l, 6n and Supplementary Figs. 1b,d, 2a,d,f,g,h, 4a, 5b, 7a-c, 8-10, 12b,c, 21a-c, 22a-c, 23a,b, 25a,b and 26 in the associated source data file. The authors declare that the remaining data are available within the Manuscript, Supplementary Information or Source Data file. Source data are provided with this paper.

ARTICLE IN PRESS

References

1 Hakim, F. E. & Farooq, A. V. Dry eye disease: an update in 2022. *The Journal of the American Medical Association* **327**, 478-479 (2022).

2 Periman, L. M., Perez, V. L., Saban, D. R., Lin, M. C. & Neri, P. The immunological basis of dry eye disease and current topical treatment options. *Journal of Ocular Pharmacology and Therapeutics* **36**, 137-146 (2020).

3 Clayton, J. A. Dry eye. *N Engl J Med* **378**, 2212-2223 (2018).

4 Han, H. *et al.* Polymer- and lipid-based nanocarriers for ocular drug delivery: Current status and future perspectives. *Adv Drug Deliv Rev* **196**, 114770 (2023).

5 Seah, I., Loh, X. J. & Su, X. A topical gel for extended ocular drug release. *Nature Biomedical Engineering* **4**, 1024-1025 (2020).

6 Bennett, N. H., Chinnery, H. R., Downie, L. E., Hill, L. J. & Grover, L. M. Material, immunological, and practical perspectives on eye drop formulation. *Advanced Functional Materials* **30**, 1908476 (2020).

7 Cui, W. *et al.* Nanoceria-mediated cyclosporin A delivery for dry eye disease management through modulating immune-epithelial crosstalk. *ACS Nano* **18**, 11084–11102 (2024).

8 Su, Y., Fan, X. & Pang, Y. Nano-based ocular drug delivery systems: an insight into the preclinical/clinical studies and their potential in the treatment of posterior ocular diseases. *Biomaterials Science* **11**, 4490-4507 (2023).

9 Shen, J. *et al.* Emerging co-assembled and sustained released natural medicinal nanoparticles for multitarget therapy of choroidal neovascularization. *Advanced Materials* **36**, 2314095 (2024).

10 Leal, J., Smyth, H. D. C. & Ghosh, D. Physicochemical properties of mucus and their impact on transmucosal drug delivery. *International Journal of Pharmaceutics* **532**, 555-572 (2017).

11 Carlson, T. L., Lock, J. Y. & Carrier, R. L. Engineering the mucus barrier. *Annu Rev Biomed Eng* **20**, 197-220 (2018).

12 Lim, B., Kim, K. S., Ahn, J. Y. & Na, K. Overcoming antibiotic resistance caused by genetic mutations of Helicobacter pylori with mucin adhesive polymer-based therapeutics. *Biomaterials* **308**, 122541 (2024).

13 TM, M. W., Lau, W. A.-O. & Khutoryanskiy, V. A.-O. Chitosan and its derivatives for application in mucoadhesive drug delivery systems. *Polymers* **10**, 267 (2018).

14 Wang, Y. *et al.* Liposome-based permeable eyedrops for effective posterior segment drug delivery. *Advanced Functional Materials* **34**, 2403142 (2024).

15 Shao, M. *et al.* Eye-Drop Nano-Formulation of Catalase Self-Assembled with Thiolated Chitosan for Effective Treatment of Dry Eye Disease. *Advanced Materials* **37**, 2415353 (2025).

16 Yang, C.-J., Anand, A., Huang, C.-C. & Lai, J.-Y. Unveiling the power of gabapentin-loaded nanoceria with multiple therapeutic capabilities for the treatment of dry eye disease. *ACS Nano* **17**, 25118-25135 (2023).

17 Kim, H., Rencoret, J., Elder, T. J., del Río, J. C. & Ralph, J. Biomimetic oxidative copolymerization of hydroxystilbenes and monolignols. *Science Advances* **9**, eade5519 (2023).

18 Zhou, T. *et al.* Rosmarinic acid-grafted gelatin nanogels for efficient diquafosol delivery in dry eye disease

ARTICLE IN PRESS

therapy. *Journal of Controlled Release* **373**, 306-318 (2024).

19 Guo, Y., Sun, Q., Wu, F.-G., Dai, Y. & Chen, X. Polyphenol-containing nanoparticles: synthesis, properties, and therapeutic delivery. *Advanced Materials* **33**, 2007356 (2021).

20 Lu, B. *et al.* Rosmarinic acid nanomedicine for rheumatoid arthritis therapy: targeted RONS scavenging and macrophage repolarization. *Journal of Controlled Release* **362**, 631-646 (2023).

21 Yang, L. *et al.* Biofilm microenvironment triggered self-enhancing photodynamic immunomodulatory microneedle for diabetic wound therapy. *Nature Communications* **14**, 7658 (2023).

22 Zhao, C. *et al.* Synthetic lignin-derived therapeutic nano reagent as intestinal pH-sensitive drug carriers capable of bypassing the gastric acid environment for colitis treatment. *ACS Nano* **17**, 811-824 (2023).

23 He, J., Ye, Y., Zhang, D., Yao, K. & Zhou, M. Visualized gallium/lyticase-integrated antifungal strategy for fungal keratitis treatment. *Advanced Materials* **34**, 2206437 (2022).

24 Deng, Z. *et al.* Metal polyphenol network/cerium oxide artificial enzymes therapeutic nanoplatform for MRI/CT-aided intestinal inflammation management. *Nano Today* **53**, 102044 (2023).

25 Soh, M. *et al.* Ceria–zirconia nanoparticles as an enhanced multi-antioxidant for sepsis treatment. *Angewandte Chemie International Edition* **56**, 11399-11403 (2017).

26 Zhou, F. *et al.* Redox homeostasis strategy for inflammatory macrophage reprogramming in rheumatoid arthritis based on ceria oxide nanozyme-complexed biopolymeric micelles. *ACS Nano* **17**, 4358-4372 (2023).

27 Kim, C. K. *et al.* Ceria nanoparticles that can protect against ischemic stroke. *Angewandte Chemie International Edition* **51**, 11039-11043 (2012).

28 Zhang, Y. *et al.* Nanozymes for nanohealthcare. *Nature Reviews Methods Primers* **4**, 36 (2024).

29 Luo, R. *et al.* Oral microsphere formulation of M2 macrophage-mimetic Janus nanomotor for targeted therapy of ulcerative colitis. *Science Advances* **10**, eado6798 (2024).

30 Saifi, M. A., Seal, S. & Godugu, C. Nanoceria, the versatile nanoparticles: promising biomedical applications. *Journal of Controlled Release* **338**, 164-189 (2021).

31 Dogru, M., Kojima, T., Simsek, C. & Tsubota, K. Potential role of oxidative stress in ocular surface inflammation and dry eye disease. *Investigative Ophthalmology & Visual Science* **59**, DES163-DES168 (2018).

32 Sies, H. Oxidative stress: a concept in redox biology and medicine. *Redox Biology* **4**, 180-183 (2015).

33 Zhou, C. *et al.* JUN is a key transcriptional regulator of the unfolded protein response in acute myeloid leukemia. *Leukemia* **31**, 1196-1205 (2017).

34 Palomer, X. *et al.* GADD45A: with or without you. *Medicinal Research Reviews* **44**, 1375-1403 (2024).

35 Liu, C. *et al.* Protein phosphatase 1 regulatory subunit 15 A promotes translation initiation and induces G2M phase arrest during cuproptosis in cancers. *Cell Death & Disease* **15**, 149 (2024).

36 Hu, C. *et al.* Heat shock proteins: biological functions, pathological roles, and therapeutic opportunities. *MedComm* **3**, e161 (2022).

37 Dubrez, L., Causse, S., Borges Bonan, N., Dumétier, B. & Garrido, C. Heat-shock proteins: chaperoning

ARTICLE IN PRESS

DNA repair. *Oncogene* **39**, 516-529 (2020).

38 Huangfu, L., Li, R., Huang, Y. & Wang, S. The IL-17 family in diseases: from bench to bedside. *Signal Transduction and Targeted Therapy* **8**, 402 (2023).

39 Prabhu, K. S. *et al.* H2AX: a key player in DNA damage response and a promising target for cancer therapy. *Biomedicine & Pharmacotherapy* **175**, 116663 (2024).

40 You, I.-C. *et al.* Macrophage phenotype in the ocular surface of experimental murine dry eye disease. *Archivum Immunologiae et Therapiae Experimentalis* **63**, 299-304 (2015).

41 Li, S. *et al.* Anti-oxidative and anti-inflammatory micelles: break the dry eye vicious cycle. *Advanced Science* **9**, 2200435 (2022).

42 Andrabi, S. M. *et al.* Nitric Oxide: physiological functions, delivery, and biomedical applications. *Advanced Science* **10**, 2303259 (2023).

43 Xiong, C. *et al.* A rabbit dry eye model induced by topical medication of a preservative benzalkonium chloride. *Investigative Ophthalmology & Visual Science* **49**, 1850-1856 (2008).

44 Agarwal, P. & Rupenthal, I. D. Modern approaches to the ocular delivery of cyclosporine A. *Drug Discovery Today* **21**, 977-988 (2016).

45 Zhang, R. *et al.* Dose-dependent benzalkonium chloride toxicity imparts ocular surface epithelial changes with features of dry eye disease. *The Ocular Surface* **18**, 158-169 (2020).

46 Zhou, T. *et al.* miR-204-containing exosomes ameliorate GVHD-associated dry eye disease. *Science Advances* **8**, eabj9617 (2022).

47 Nagai, N. & Otake, H. Novel drug delivery systems for the management of dry eye. *Advanced Drug Delivery Reviews* **191**, 114582 (2022).

48 Yang, F. M. *et al.* The artemisinin analog SM934 alleviates dry eye disease in rodent models by regulating TLR4/NF-κB/NLRP3 signaling. *Acta Pharmacologica Sinica* **42**, 593-603 (2021).

49 Chaudhari, P. *et al.* Rodent models for dry eye syndrome: standardization using benzalkonium chloride and scopolamine hydrobromide. *Life Sciences* **317**, 121463 (2023).

50 Singh, S., Sharma, S. & Basu, S. Rabbit models of dry eye disease: current understanding and unmet needs for translational research. *Experimental Eye Research* **206**, 108538 (2021).

51 Hu, S. *et al.* A mussel-inspired film for adhesion to wet buccal tissue and efficient buccal drug delivery. *Nature Communications* **12**, 1689 (2021).

52 Poinard, B., Kamaluddin, S., Tan, A. Q. Q., Neoh, K. G. & Kah, J. C. Y. Polydopamine coating enhances mucopenetration and cell uptake of nanoparticles. *ACS Applied Materials & Interfaces* **11**, 4777-4789 (2019).

Acknowledgments

ARTICLE IN PRESS

Financial support from the Zhejiang Province Key Research and Development Program (2024C03073 received by H. H.), National Natural Science Foundation of China (22375128 received by Y. W., 82572387 received by H. H., 82271064 received by H. H., 22105126 received by Y. W.), and the Zhejiang Province Natural Science Foundation (LR23H120001 received by H. H.) is acknowledged.

Author contributions

Z. W., Z. L., H. H., and Y. W. conceived the project and designed the experiments. Z. W. and R. X. synthesized materials. Z. W. and Y. G. performed in vitro cell experiments. Z. L. performed in vivo experiments. Z. W., Z. L., R. X., F. W., H. H., and Y. W. contributed to data collection and analysis. Z. W., Z. L., H. H., and Y. W. cowrote the manuscript. All authors discussed the results and reviewed the manuscript.

Competing interests

The authors declare no competing interests.

ARTICLE IN PRESS

Figure legends

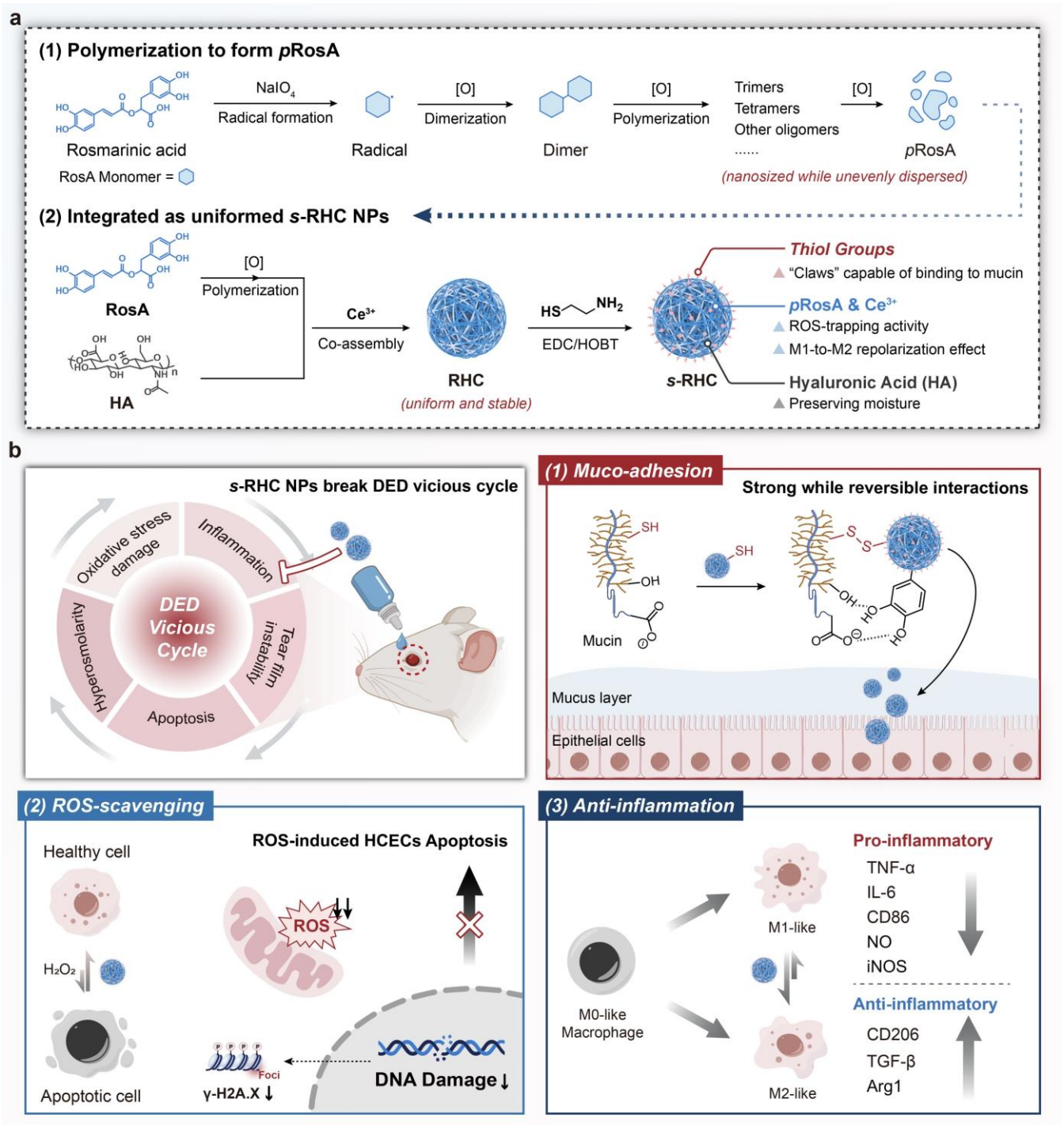

Fig. 1. Scheme for the fabrication of *s*-RHC NPs and therapeutic mechanisms for DED. a Scheme for the preparation of *s*-RHC NPs. **b** Illustration of engineering muco-adhesive *s*-RHC NPs for DED treatments and their specific therapeutic mechanisms. The scheme created in BioRender. Wang, Z. (2026) (https://BioRender.com/i62ypzs) is licensed under CC BY 4.0.

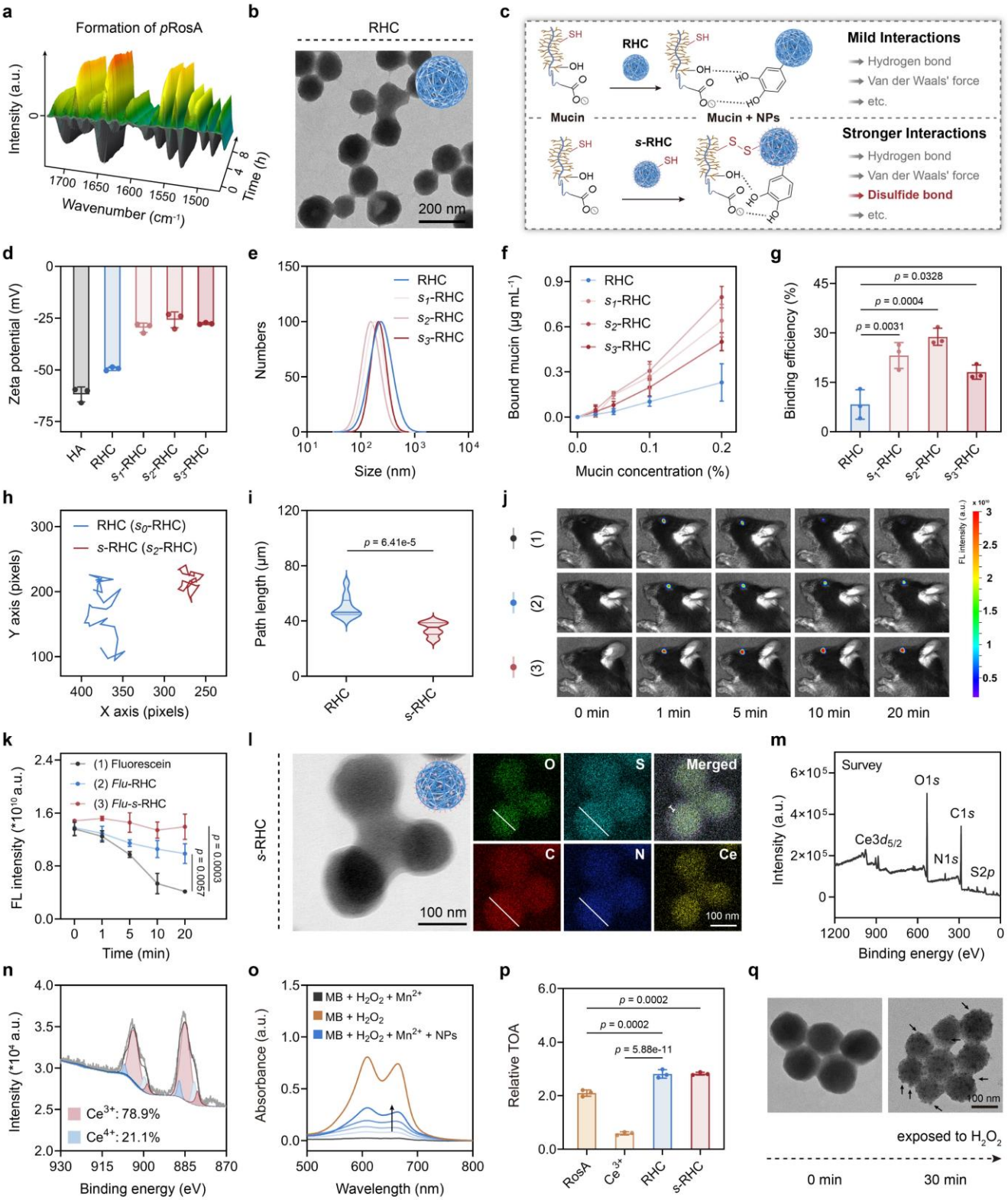

Fig. 2. Characterizations of the RHC NPs and three thiolated RHC NPs. a In situ FTIR spectra (1450 cm^{-1} ~ 1750 cm^{-1}) detecting the polymerization of RosA into *p*RosA. **b** Representative TEM image and simulated image (inset) of RHC NPs. Scale bar = 200 nm. **c** Scheme illustrating the potential interactions between NPs and mucin.

ARTICLE IN PRESS

d Zeta potentials of RHC NPs and thiolated RHC NPs (n = 3 independent samples; mean ± SD). **e** Hydrodynamic size distributions of RHC NPs and three thiolated RHC NPs. **f** Amount of bound mucin by different NPs in the presence of the mucin at different concentrations detected by Bradford assay (n = 3 independent samples; mean ± SD). **g** Mucin binding efficiency of NPs when the concentration of mucin was 0.1% (n = 3 independent samples; mean ± SD). **h** Representative trajectories of RHC NPs and *s*-RHC NPs incubated with mucin solutions within 15 s. **i** Accumulated path lengths of NPs incubated with mucin solutions (n = 10 independent samples; mean ± SD). **j** Evaluation of the precorneal retention of NPs was conducted using real-time in vivo fluorescence imaging. Groups are assigned to be: (1) Fluorescein, (2) *Flu*-RHC, (3) *Flu*-*s*-RHC. **k** Quantitative analyses of changes in fluorescence intensity of in vivo fluorescence imaging (n = 3 independent biological samples; mean ± SD). **l** Representative TEM image, simulated image (inset), and elemental mapping images of *s*-RHC NPs. Scale bars = 100 nm. **m** The XPS survey spectrum, and (**n**) XPS spectra of Ce3*d* in *s*-RHC NPs (a.u. refers to arbitrary units). **o** UV-vis spectra of MB aqueous solutions with different treatments. **p** Relative total antioxidant capacity (compared with the antioxidant capacity of Fe^{2+}) of different formulations (n = 3 independent samples; mean ± SD). **q** Morphological changes of *s*-RHC NPs incubated with 200 μM H_2O_2 for 30 min. Black arrows highlight the smaller spheres distributed on the surface of NPs. Scale bar = 100 nm. In (**b**), (**j**), and (**q**), the experiments were repeated independently three times with similar results, and a representative result is shown for each. Statistical analyses of (**g**) and (**p**) were processed by two-sided one-way analysis of variance (ANOVA) with Tukey's multiple comparisons test; (**i**) was calculated a two-sided, unpaired Student's *t* test. Source data are provided as a Source Data file. Scheme of (**c**) created in BioRender. Wang, Z. (2026) (https://BioRender.com/i62ypzs) is licensed under CC BY 4.0.

ARTICLE IN PRESS

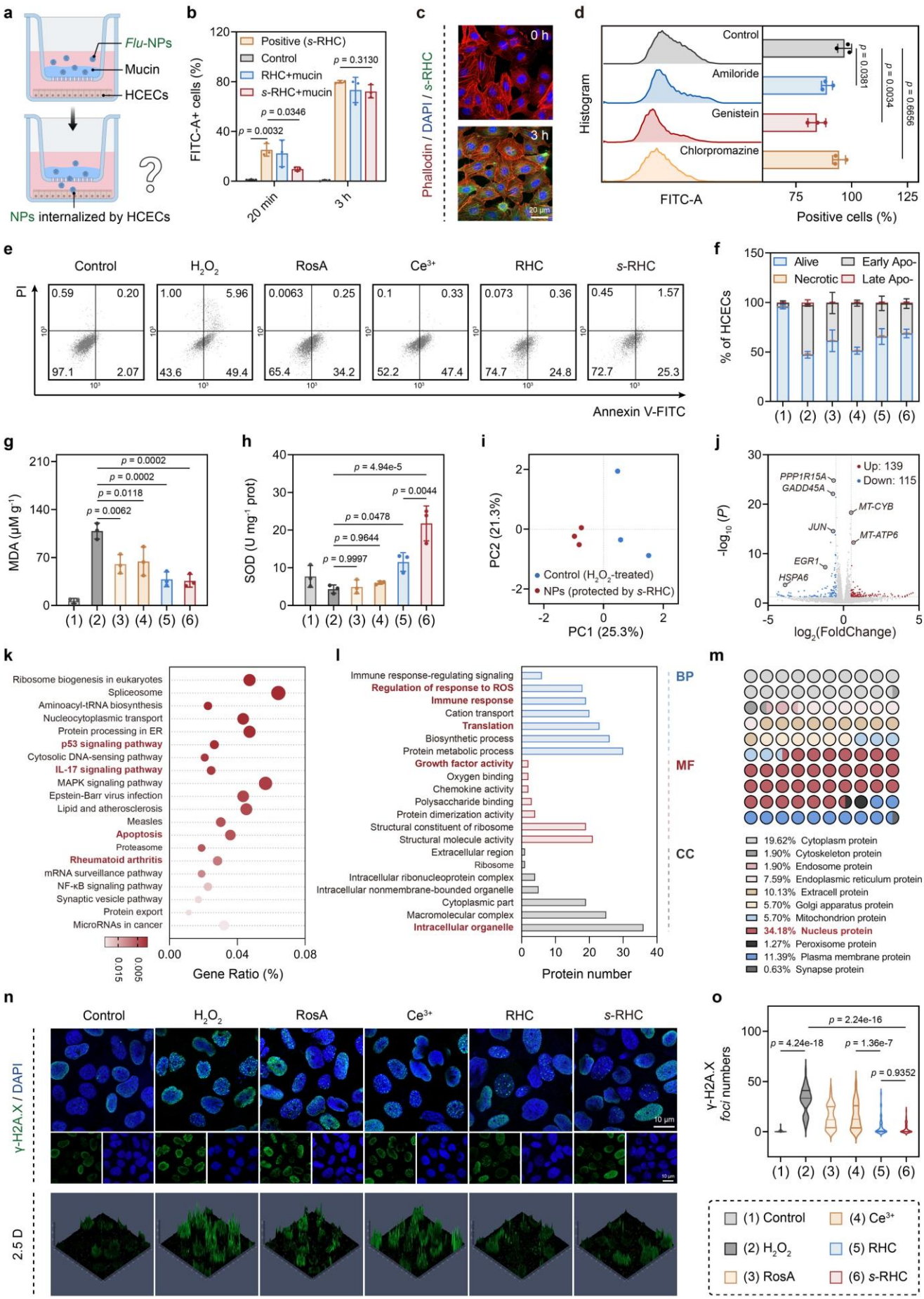
a
Flu-NPs
Mucin
HCECs
NPs internalized by HCECs
b
Positive (s-RHC)
Control
RHC+mucin
s-RHC+mucin
FITC-A+ cells (%)
p = 0.0032
p = 0.0346
p = 0.3130
20 min
3 h
c
Phallodin / DAPI / s-RHC
0 h
3 h
20 μm
d
Histogram
Control
Amiloride
Genistein
Chlorpromazine
FITC-A
p = 0.0381
p = 0.0034
p = 0.6656
Positive cells (%)
e
Control
H2O2
RosA
Ce3+
RHC
s-RHC
PI
0.59 0.20 97.1 2.07
1.00 5.96 43.6 49.4
0.0063 0.25 65.4 34.2
0.1 0.33 52.2 47.4
0.073 0.36 74.7 24.8
0.45 1.57 72.7 25.3
Annexin V-FITC
f
Alive
Early Apo-
Necrotic
Late Apo-
% of HCECs
(1) (2) (3) (4) (5) (6)
g
MDA (μM g-1)
p = 0.0002
p = 0.0002
p = 0.0118
p = 0.0062
h
SOD (U mg-1 prot)
p = 4.94e-5
p = 0.0044
p = 0.0478
p = 0.9644
p = 0.9997
i
PC2 (21.3%)
PC1 (25.3%)
Control (H2O2-treated)
NPs (protected by s-RHC)
j
Up: 139
Down: 115
PPP1R15A
GADD45A
MT-CYB
JUN
MT-ATP6
EGR1
HSPA6
-log10 (P)
log2(FoldChange)
k
Ribosome biogenesis in eukaryotes
Spliceosome
Aminoacyl-tRNA biosynthesis
Nucleocytoplasmic transport
Protein processing in ER
p53 signaling pathway
Cytosolic DNA-sensing pathway
IL-17 signaling pathway
MAPK signaling pathway
Epstein-Barr virus infection
Lipid and atherosclerosis
Measles
Apoptosis
Proteasome
Rheumatoid arthritis
mRNA surveillance pathway
NF-κB signaling pathway
Synaptic vesicle pathway
Protein export
MicroRNAs in cancer
Gene Ratio (%)
l
BP
MF
CC
Immune response-regulating signaling
Regulation of response to ROS
Immune response
Cation transport
Translation
Biosynthetic process
Protein metabolic process
Growth factor activity
Oxygen binding
Chemokine activity
Polysaccharide binding
Protein dimerization activity
Structural constituent of ribosome
Structural molecule activity
Extracellular region
Ribosome
Intracellular ribonucleoprotein complex
Intracellular nonmembrane-bounded organelle
Cytoplasmic part
Macromolecular complex
Intracellular organelle
Protein number
m
19.62% Cytoplasm protein
1.90% Cytoskeleton protein
1.90% Endosome protein
7.59% Endoplasmic reticulum protein
10.13% Extracell protein
5.70% Golgi apparatus protein
5.70% Mitochondrion protein
34.18% Nucleus protein
1.27% Peroxisome protein
11.39% Plasma membrane protein
0.63% Synapse protein
n
Control
H2O2
RosA
Ce3+
RHC
s-RHC
γ-H2A.X / DAPI
2.5 D
10 μm
o
γ-H2A.X foci numbers
p = 2.24e-16
p = 4.24e-18
p = 1.36e-7
p = 0.9352
(1) Control
(2) H2O2
(3) RosA
(4) Ce3+
(5) RHC
(6) s-RHC

ARTICLE IN PRESS

Fig. 3. ROS-scavenging and cyto-protective capability of *s*-RHC NPs. a Schematic diagram of HCECs monolayer transwell experiments mimicking the interactions between fluorescein-labelled NPs and ocular surface. **b** Flow cytometry quantification of internalized formulations in HCECs cultured in transwell at various time points (n = 3 independent biological samples; mean ± SD). Details of group assignments are shown in Supplementary Fig. 11. **c** Fluorescence images of endocytosis of fluorescein-labelled *s*-RHC NPs by HCECs. Scale bar = 20 μm. **d** Cell uptake efficacy of HCECs treated with different inhibitors by flow cytometry and the quantitative analysis (n = 3 independent biological samples; mean ± SD). **e** Flow cytometry results for the apoptosis of HCECs treated with different groups stained by annexin V-fluorescein isothiocyanate (FITC) and propidium iodide (PI). **f** Quantitative analyses of flow cytometry for the apoptosis of HCECs treated with different groups (n = 3 independent biological samples; mean ± SD). Groups are assigned to be: (1) Control, (2) H_2O_2, (3) RosA, (4) Ce^{3+}, (5) RHC, (6) *s*-RHC. **g** Intracellular MDA levels, and (**h**) intracellular SOD activities after different treatments (n = 3 independent biological samples; mean ± SD). **i** PCA analysis presenting differentially expressed genes expressed by H_2O_2-treated HCECs with or without *s*-RHC treatments (termed as “NPs” and” Control”), respectively. **j** Volcano plot illustrating differential genes expressed by different samples. **k** Scatterplot of KEGG enrichment showing differentially enriched signaling pathways. The size and color of the dots represent the gene ratio and *p* value, respectively. **l** GO functional annotation analysis of the proteins in HCECs. The functional annotation was categorized into cellular component (CC), molecular function (MF), and biological process (BP), with each domain ranking based on the number of proteins. **m** Subcellular localization analysis showing the intracellular distribution of all identified proteins in HCECs. **n** Fluorescence images of γ-H2A.X foci (green) in cell nuclei (blue) of HCECs after different treatments and (**o**) the statistics of γ-H2A.X foci (n = 50 independent biological samples; mean ± SD). Scale bars = 10 μm. In (**c**), the experiments were repeated independently three times with similar results; whereas in (**n**), the experiments were repeated independently until 50 nuclei of cells were collected, and a representative result is shown for each. Statistical analyses were processed by two-tailed one-way ANOVA with Tukey’s multiple comparisons test. The full names of gene abbreviations are shown in Supplementary Table 1. Source data are provided as a Source Data file. Scheme of (**a**) created in BioRender. Wang, Z. (2026) (https://BioRender.com/i62ypzs) is licensed under CC BY 4.0.

ARTICLE IN PRESS

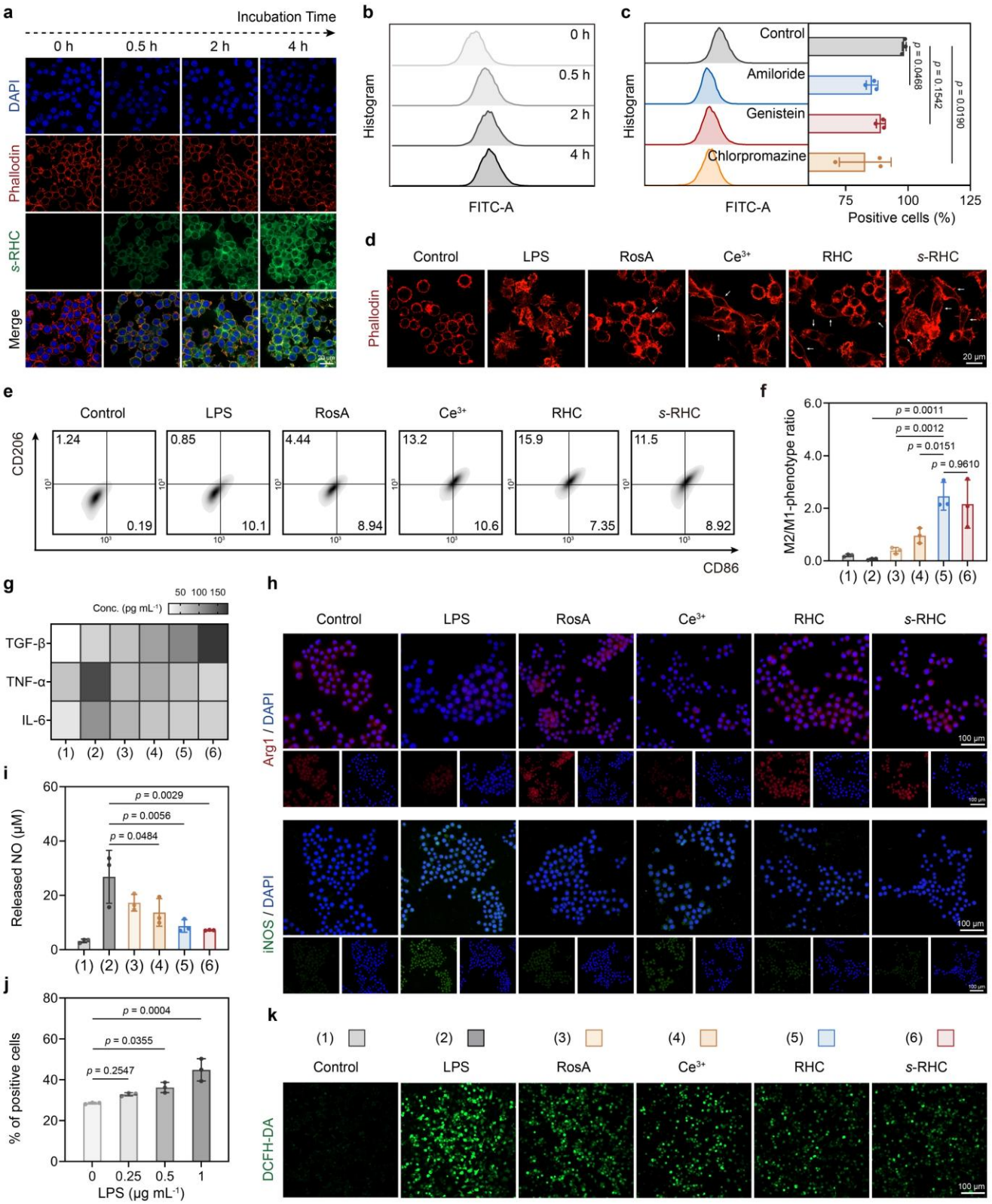

Fig. 4. M1-to-M2 repolarization effect of *s*-RHC NPs. a Time-dependent endocytosis of fluorescein-labelled *s*-RHC NPs by RAW264.7 cells, and (**b**) the corresponding flow cytometry results. Scale bar = 20 μm. **c** Cell uptake efficacy of RAW264.7 cells treated with different inhibitors by flow cytometry and the quantitative analysis (n = 3

ARTICLE IN PRESS

independent biological samples; mean ± SD). **d** Cytoskeleton staining images of RAW264.7 cells treated with different formulations. Scale bar = 20 μm. The spindle shaped RAW264.7 cells are highlighted by white arrows. **e** Populations of M1-like ($CD86^+/CD206^-$) and M2-like ($CD86^-/CD206^+$) macrophages were analyzed by flow cytometry after different treatments. **f** Quantitative analyses of flow cytometry for populations of M1-like and M2-like macrophages (n = 3 independent biological samples; mean ± SD). Groups are assigned to be: (1) Control, (2) LPS, (3) RosA, (4) Ce^{3+}, (5) RHC, (6) *s*-RHC. **g** Heatmap illustrating the ELISA results of secreted TGF-β, TNF-α, and IL-6 after different treatments (n = 3 independent biological samples; mean ± SD). **h** Representative immunofluorescence staining of Arg1 (red), iNOS (green), and cell nuclei (blue). Scale bars = 100 μm. **i** NO release from RAW264.7 cells detected by Griess assays (n = 3 independent biological samples; mean ± SD). **j** Quantitative analysis of intracellular ROS levels in RAW264.7 cells treated with varying LPS concentrations by flow cytometry (n = 3 independent biological samples; mean ± SD). **k** Representative DCFH-DA fluorescence staining of RAW264.7 cells after different treatments. Scale bar = 100 μm. In (**a**), (**d**), (**h**) and (**k**), the experiments were repeated independently three times with similar results, and a representative result is shown for each. Statistical analyses were processed by two-tailed one-way ANOVA with Tukey's multiple comparisons test. Source data are provided as a Source Data file.

ARTICLE IN PRESS

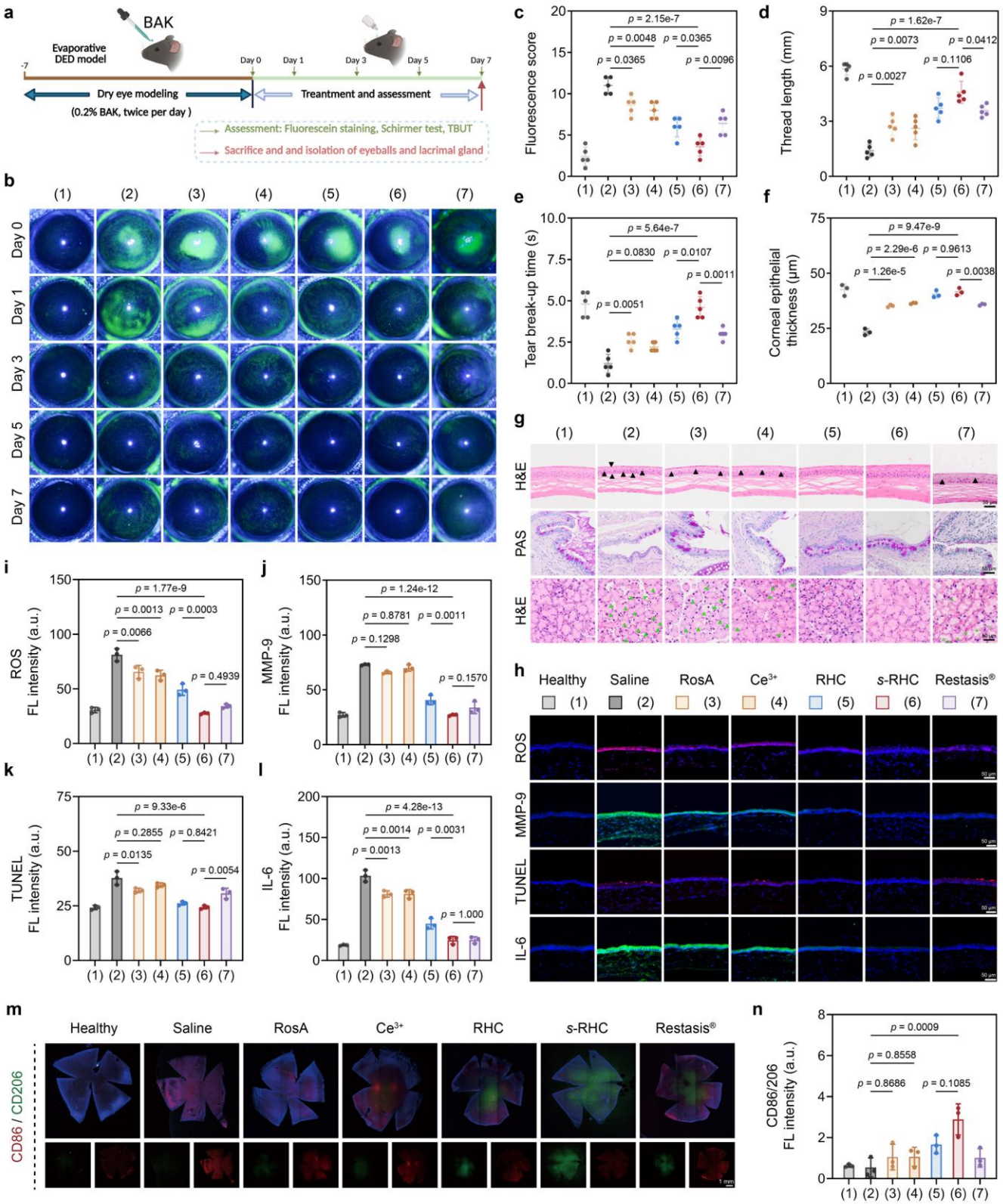

Fig. 5. Therapeutic efficacy of *s*-RHC in the evaporative DED models. a Schematic representation of the establishment, treatment procedure, and treatment evaluation of the evaporative DED model. **b** Representative corneal fluorescein-stained images, and (**c**) their fluorescein scores according to a 0-4-point system of the ocular

ARTICLE IN PRESS

surface on Day 7 (n = 5 independent biological samples; mean ± SD). **d** Statistical data of tear volume through the Schirmer test after various treatments on Day 7 (n = 5 independent biological samples; mean ± SD). **e** Quantitative statistical plots of tear break-up time after different treatments on Day 7 (n = 5 independent biological samples; mean ± SD). **f** Quantitative data of the corneal epithelium thickness on Day 7 (n = 3 independent biological samples; mean ± SD). **g** Representative images of H&E staining of the cornea (upper) and the lacrimal gland (lower), the conjunctiva structure and goblet cell numbers are visualized through PAS staining. Black triangles marked out the abnormal epithelial cells, and green triangles marked out the vacuoles in the acins. Scale bars = 50 μm. **h** Evaluations of ROS, MMP-9, TUNEL, and IL-6 by immunostaining of corneal epithelium. Scale bars = 50 μm. **i** Quantitative assessment of the overall fluorescence intensity of ROS, (**j**) MMP-9, (**k**) TUNEL, and (**l**) IL-6 (n = 3 independent biological samples; mean ± SD). **m** The corneal whole-mount and immunofluorescent staining of evaporative DED mice treated with different formulations (blue, DAPI; green, CD206; red, CD86). Scale bar = 1 mm. **n** Quantitative assessment of fluorescent intensity of corneal whole-mount and immunofluorescent staining (n = 3 independent biological samples; mean ± SD). Groups are assigned to be: (1) Healthy, (2) Saline, (3) RosA, (4) Ce^{3+}, (5) RHC, (6) *s*-RHC, (7) Restasis®. In (**b**), the experiments were repeated independently five times with similar results; whereas in (**g**), (**h**) and (**m**), the experiments were repeated independently three times with similar results, and a representative result is shown for each. Statistical analyses were processed by two-tailed one-way ANOVA with Tukey's multiple comparisons test. Source data are provided as a Source Data file. Scheme of (**a**) created in BioRender. Wang, Z. (2026) (https://BioRender.com/i62ypzs) is licensed under CC BY 4.0.

ARTICLE IN PRESS

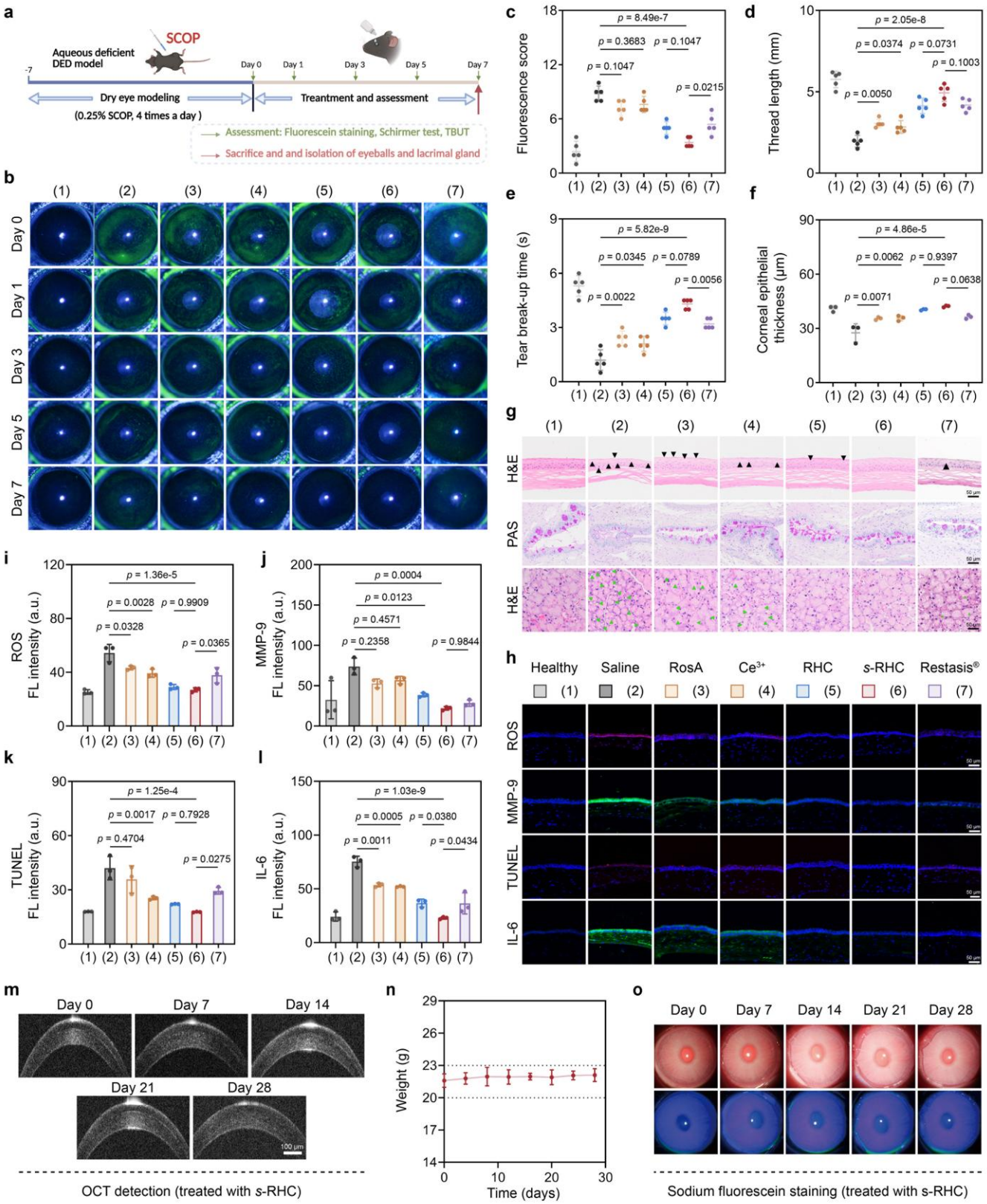

Fig. 6. Therapeutic efficacy of *s*-RHC on the aqueous deficient DED models. a Schematic representation of the establishment, treatment procedure, and treatment evaluation of the aqueous deficient DED model. **b**

ARTICLE IN PRESS

Representative corneal fluorescein-stained images, and (**c**) their fluorescein scores according to a 0-4-point system of the ocular surface on Day 7 (n = 5 independent biological samples; mean ± SD). **d** Statistical data of tear volume through the Schirmer test after various treatments on Day 7 (n = 5 independent biological samples; mean ± SD). **e** Quantitative statistical plots of tear break-up time after different treatments on Day 7 (n = 5 independent biological samples; mean ± SD). **f** Quantitative data of the corneal epithelium thickness on Day 7 (n = 3 independent biological samples; mean ± SD). **g** Representative images of H&E staining of the cornea (upper) and the lacrimal gland (lower), the conjunctiva structure and goblet cell numbers are visualized through PAS staining. Black triangles marked out the abnormal epithelial cells, and green triangles marked out the vacuoles in the acins. Scale bars = 50 μm. **h** Evaluations of ROS, MMP-9, TUNEL, and IL-6 by immunostaining of corneal epithelium. Scale bars = 50 μm. **i** Quantitative assessment of the overall fluorescence intensity of ROS, (**j**) MMP-9, (**k**) TUNEL, and (**l**) IL-6 (n = 3 independent biological samples; mean ± SD). **m** Representative anterior segment optical coherence tomography (OCT) images of cornea after administration of *s*-RHC NPs for 28 days. Scale bar = 100 μm. **n** Records of body weights of mice treated with *s*-RHC NPs at Day 0, 4, 8 12, 16, 20, 24 and 28 (n = 3 independent biological samples; mean ± SD). **o** Ocular irritation test of rabbits under slit lamp observation at Day 0, 7, 14, 21 and 28 after the topical instillation of *s*-RHC NPs. Groups are assigned to be: (1) Healthy, (2) Saline, (3) RosA, (4) Ce^{3+}, (5) RHC, (6) *s*-RHC, (7) Restasis®. In (**b**), the experiments were repeated independently five times with similar results; whereas in (**g**), (**h**), (**m**), and (**o**), the experiments were repeated independently three times with similar results, and a representative result is shown for each. Statistical analyses were processed by two-tailed one-way ANOVA with Tukey's multiple comparisons test. Source data are provided as a Source Data file. Scheme of (**a**) created in BioRender. Wang, Z. (2026) (https://BioRender.com/i62ypzs) is licensed under CC BY 4.0.

ARTICLE IN PRESS

Editor Summary:

Ocular inflammation is involved in the pathology of several eye disease. Here, the authors on cerium complexed self-polymerised rosmarinic acid-hyaluronic acid nanoparticles with thiol modification for eye retention to reduce oxidative stress and inflammation in dry eye disease.

Peer Review Information:

Nature Communications thanks Chengchao Chu and the other anonymous reviewers for their contribution to the peer review of this work. [A peer review file is available.]